ASSESSMENT OF UNDERSAMPLING STRATEGIES FOR ACCELERATED MULTI-SHELL DIFFUSION MRI

A THESIS SUBMITTED TO

THE GRADUATE SCHOOL OF ENGINEERING AND SCIENCE

OF BILKENT UNIVERSITY

IN PARTIAL FULFILLMENT OF THE REQUIREMENTS FOR

THE DEGREE OF

MASTER OF SCIENCE

IN

ELECTRICAL AND ELECTRONICS ENGINEERING

By
Elif Aygün
August 2022

Assessment of Undersampling Strategies for Accelerated Multi-Shell
Diffusion MRI
By Elif Aygün
August 2022

We certify that we have read this thesis and that in our opinion it is fully adequate,
in scope and in quality, as a thesis for the degree of Master of Science.

—————————
Emine Ülkü Sarıtaş Çukur(Advisor)

—————————————
Hatice Kader Karlı Oğuz

—————————————
Tolga Çukur

Approved for the Graduate School of Engineering and Science:

————
Orhan Arıkan
Director of the Graduate School

ABSTRACT

ASSESSMENT OF UNDERSAMPLING STRATEGIES FOR ACCELERATED MULTI-SHELL DIFFUSION MRI

Elif Aygün
M.S. in Electrical and Electronics Engineering
Advisor: Emine Ülkü Sarıtaş Çukur
August 2022

Diffusion Magnetic Resonance Imaging (dMRI) is a non-invasive imaging technique that can probe the Brownian motion of water molecules within the neurite tissue. Measuring diffusion in the brain by densely sampling the q-space allows quantification of neural microstructure characteristics on a much smaller scale than the regular imaging resolution. Diffusion Tensor Imaging (DTI), which can resolve diffusion anisotropy and primary fiber orientation, is one of the most clinically adopted dMRI techniques. However, white matter (WM) voxels in the brain often contain crossing fibers and complex neurite structures, requiring more sophisticated dMRI techniques. With the goal of resolving multiple diffusion orientations and increasing angular resolution, multi-shell High Angular Resolution Diffusion Imaging (HARDI) samples the q-space densely on multiple spherical surfaces with radii determined by the b-values. This technique allows inferring neurite characteristics of complex fiber bundles, enabling the diagnosis of many neurodegenerative diseases. This thesis focuses on two multi-shell dMRI methods: Multi-Shell Multi-Tissue Constrained Spherical Deconvolution (MSMT-CSD), a model-free method, and Neurite Orientation Dispersion and Density Imaging (NODDI), a model-based method. These methods are used to resolve the Orientation Distribution Function (ODF) and Orientation Dispersion (OD) in the brain. However, the requirement of high number of q-space measurements, combined with the need to acquire images with reversed phase encoding (PE) directions for susceptibility artifact correction, causes prolonged acquisition times and reduces the clinical utility of multi-shell dMRI.

This thesis proposes several different undersampling strategies to accelerate multi-shell dMRI, and compares their performances based on the quality of estimated dMRI metrics and ODFs. The first undersampling approach is directly applied to the q-space using Electrostatic Energy Minimization (EEM) to produce

2- or 3-shell schemes with different combinations of gradient directions per shell. The second approach uses acquisitions with reversed PE directions for a single b0 volume only. These strategies are applied to achieve acceleration rates of R=2 and R=3 on dMRI data from 20 subjects. The results suggest that each diffusion metric prefers a different undersampling strategy. For R=2 case, 3-shell strategies perform better in terms of metric fidelity and ODF accuracy. Specifically, gradient tables with a lower variance in the number of q-space points between consecutive shells are preferable. For R=3 case, 2-shell strategies perform better and the strategies containing more gradient points on the outer shell are preferable. The metric maps produced from the undersampled data contain all the necessary microstructural information and preserve diagnostic properties. These analyses will be useful in designing disease and metric-specific multi-shell dMRI gradient tables to ease clinical applications and shorten the acquisition time with minimum loss of information.

ÖZET

HIZLANDIRILMIŞ ÇOKLU-KABUK DİFÜZYON MRG İÇİN ALT-ÖRNEKLEME STRATEJİLERİNİN DEĞERLENDİRİLMESİ

Elif Aygün

Elektrik ve Elektronik Mühendisliği, Yüksek Lisans

Tez Danışmanı: Emine Ülkü Sarıtaş Çukur

Ağustos 2022

Difüzyon manyetik rezonans görüntüleme (dMRG), su moleküllerinin nöral doku boyunca gerçekleştirdiği Brown hareketine duyarlı noninvaziv bir görüntüleme yöntemidir. Beyinde gerçekleşen difüzyonun, q-uzayının farklı yörüngelerle örneklenmesiyle ölçülmesi, dokunun mikroyapısal özelliklerinin standart görüntüleme çözünürlüğünden çok daha hassas ölçeklerle çözümlenebilmesini sağlamaktadır. Difüzyon Tensor Görüntüleme (DTG) klinikte en yaygın olarak kullanılan dMRG yöntemidir ve difüzyon anizotropisiyle birincil lif yönelimini çözümleyebilmektedir. Ancak beyinde gözlemlenen karmaşık lif yapılarının görüntülenmesi için birden fazla difüzyon yönelimi için çalışacak teknikler gerekmektedir. Yüksek Açısal Çözünürlüklü Difüzyon Görüntüleme (HARDI), q-uzayını olabildiğince yoğun bir alt örnekleme yapısıyla kapsayarak açısal çözünürlüğü arttıran bir tekniktir. Çoklu-Kabuk HARDI teknikleri, q-uzayını yarı çapı b-değerince belirlenen küresel yüzeyler üzerinde örnekler ve karmaşık lif yapılarının çözülmesine olanak sağlayarak pek çok nörodejeneratif hastalığın teşhisine imkan tanır. Bu tez iki farklı çoklu-kabuk dMRG yöntemine odaklanmaktadır: Modelden bağımsız bir yöntem olan Çoklu-Doku Çoklu-Kabuk Kısıtlı Küresel Ters Evrişim (ÇDÇK-KKTE), ve difüzyon modeli tabanlı bir teknik olan Nörit Oryantasyon Dağılımı ve Yoğunluk Görüntüleme (NODDI). Bu iki yöntem, beyindeki Yönelim Dağılım Fonksiyonunu (YDF) ve Yönelim Yayılımını (YY) çözümlemek için kullanılmaktadır. Bu yöntemlerin kullanılması için gerekli olan yüksek sayıdaki q-uzayı ölçümleri ve difüzyon görüntülerinde manyetik alınganlık kaynaklı bozulmaların düzeltilmesi için zıt faz kodlama yönlerinde görüntüler alınması gerekliliği, çoklu-kabuk HARDI protokollerinin çok uzun sürmesine sebep olmakta ve yöntemin klinik kullanım için uygunluğunu düşürmektedir.

Bu tezde, çoklu-kabuk dMRG protokollerinin hızlandırılması için farklı alt-örnekleme stratejileri önerilmekte, ve bu stratejilerle elde edilen metrik haritalarının ve YDF'nin doğruluğu karşılaştırılmaktadır. Önerilen ilk alt-örnekleme yöntemi, q-uzayındaki her bir kabuğun Elektrostatik Enerji Enazlaması (EEE) yöntemi ile farklı oranlarda alt örneklenilerek yeni 2-kabuklu ya da 3-kabuklu gradyan tablolarının oluşturulmasıdır. İkinci yöntem ise zıt faz kodlama yönünde yalnızca tek bir b0 görüntüsü kullanmaktadır. Bu stratejiler, 20 gönüllü için dMRG verisinin R=2 ve R=3 seviyelerinde hızlandırılması için uygulanmıştır. Sonuçlar her bir metrik için en iyi performans gösteren alt örnekleme stratejisinin farklı olduğunu belirtmektedir. R=2 için 3-kabuklu stratejiler dMRG metriklerinin ve YDF'nin doğruluğu açısından daha iyi performans göstermektedir. Genellikle birbirini takip eden iki kabuk arasında gradyan noktası sayısı değişimi az olan stratejiler daha başarılıdr. R=3 için 2-kabuklu stratejiler daha başarılıdr ve dış kabuklarda daha çok sayıda gradyan noktası barındıran stratejiler diğerlerinden daha üstündür. Tüm stratejiler altında metrik haritaları, mikroyapısal özellikleri içermekte ve teşhis için önemli özellikleri korumaktadır. Bu analizler, çoklu-kabuk dMRG gradyan tabolarının hastalığa ve hedeflenilen metriğe özel tasarlanması ile klinik uygulamaların kolaylaştırılmasında, ve minimum bilgi kaybıyla veri toplama süresinin kısaltılmasında faydalı olacaktır.

Anahtar sözcükler: Difüzyon manyetik rezonans görüntüleme, çoklu-kabuk difüzyon görüntüleme, alt örnekleme, q-uzayı, b-değeri, difüzyon metrikleri.

Acknowledgement

Before I start, I would like to acknowledge that this thesis was supported Scientific and Technological Research Council of Turkey (TUBITAK Grant No: 117E116).

As I am completing my Master's thesis and looking back on these three years full of research, hard work, and dedication, I can say that I am happy that I decided to pursue an M.Sc. degree at Bilkent University under the supervision of Assoc. Prof Emine Ülkü Sarıtaş. I couldn't even explain how this process transformed and matured me. I always knew that I wanted to contribute to medical technologies, and I believe medical imaging, especially MRI research, was an excellent fit. I am very excited to continue working in this field.

I want to start by thanking Assoc. Prof Emine Ülkü Sarıtaş for her immense contribution and guidance during these three years. I first started working with her during my summer internship, which strongly shaped my career aspirations. She was incredibly supportive and helpful, and with her knowledge and expertise, she guided me, even when I was very confused about the research. I am very thankful for her empathy, support, and positive attitude, and I cannot appreciate her enough as an advisor.

I had the chance of meeting and working with the most incredible people during my time at UMRAM. Mahmut and Bahadır were terrific people I met and became great friends of mine. I am glad I got to meet Abdallah, with who I had the pleasure of working together and defending our point of view against Bahadır. Aslı and Beril are very kind and positive people. Rahmi, with unending patience, helped me with my never-ending 3D-printing journey. Alper is one of the most positive and helpful people I met and with whom I enjoyed talking. Mustafa is very supportive, helpful, and kind, I am still amazed by his contributions to our lab. I am also incredibly grateful for meeting Ecrin, Bilal, Semih, and Tunç, who became great companions. I am also fortunate to have the chance to meet and work with Prof. Kader Karlı Oğuz, and she is one of the most talented, knowledgeable people that supported me while we were contributing together.

I am beyond grateful for the support of my dearest friends. They uplifted me when I was at my lowest and always listened to my complaints about the things I couldn't figure out during my research, even though they didn't understand a word. Irmak always consoled and supported me, believing that I was capable of anything and everything. Deniz gleefully spent her time with me; we watched many movies together and talked about them non-stop. Yağız was there whenever I needed, even when I was irrationally mad or sad about my work. Bora was constant support along the way, as he was seven years old; I will never forget how he comes out of his night shifts with just 1 hour of sleep to meet me and casually talks about the brain surgery he just attended. İpek and Gökhan were always there for me in our Zoom meetings since we are so bad at scheduling an in-person get-together suitable for all of us. Ece and Dila, my dearest friends, uplifted, celebrated, listened to and supported me as they always did since we were little girls. I cannot thank them enough.

Also, I would like to thank my father Ali, mother Serap, and sister Işıl. They are my greatest source of pride, and I could not do this without their support. I am unsure if they still don't know what I am working on, but they are constantly amazed by my work, celebrating and comforting me. Işıl, although being an architecture student, even read this thesis with utmost seriousness, was there with me every step of the way. I don't even know what I would do without her support. Finally, I think Yuta, my gentle-hearted cat, who hates me a little and beats me with great passion at every chance he gets but still follows me around everywhere I go, was a fantastic late-night study companion. I am incredibly grateful for my family and their support.

It was a great pleasure working with Prof. Sarıtaş at UMRAM, and these three years was a great opportunity. Hoping that one day, the UMRAM lane in the woods would get illuminated...

Contents

List of Figures

Chapter 1

Introduction

Diffusion Magnetic Resonance Imaging (dMRI) is a non-invasive imaging technique that can probe Brownian motion of water molecules within the neurite tissue [1, 2]. The measurement of diffusion in the brain gives dMRI a unique ability to resolve the underlying microstructure of neurite tissue. The information can be used to characterize and quantify diffusion and structural properties of fiber bundles on a much smaller scale than the regular imaging resolution.

The fibers in neurite tissue biologically restrict the diffusion process, such that the water molecules randomly move along the fiber or in between the fibers [2]. The diffusion process depends on the environment, allowing one to map the microstructural alignment of the white matter (WM) axons, as well as gray matter (GM) and cerebrospinal fluid (CSF) tissue properties.

MRI pulse sequences can be sensitized to diffusion by applying a pair of gradient fields that induce a signal attenuation in the case of random spin motion [3, 1].The most common dMRI technique using such diffusion-sensitizing gradients is Diffusion Tensor Imaging (DTI), which relies on q-space measurements acquired in at least 6 gradient directions and 1 non-diffusion-weighted measurement to construct a diffusion tensor. From there, two important metrics called Fractional Anisotropy (FA) and Mean Diffusivity (MD) can be computed [1].

However, DTI fails to resolve complex fiber geometries, often seen in WM brain voxels. Therefore, more sophisticated techniques with the capability to resolve multiple fiber orientations are needed.

High Angular Resolution Diffusion Imaging (HARDI) was developed to overcome the crossing-fibers problem by sampling the q-space as densely as possible in different trajectories [4, 2]. Multi-shell HARDI is an extension of HARDI, where the q-space is sampled on multiple spherical surfaces whose radii are determined by the b-values. These spherical surfaces are called "shells" and this method simultaneously allows us to benefit from both the high angular resolution of high b-values and high Signal to Noise Ratio (SNR) of low b-values [2]. Using the signal attenuation measured with multi-shell HARDI, the diffusion distribution can be estimated by reconstructing the Orientation Distribution Function (ODF) or Orientation Dispersion (OD) using either model-free or model-based approaches. This thesis considers the following multi-shell dMRI methods: (1) Multi-Shell Multi-Tissue Constrained Spherical Deconvolution (MSMT-CSD) is a model-free technique, with metrics of Apparent Fibre Density (AFD) and number of Fiber Orientations (nuFO) metrics[5]. (2) Neurite Orientation Dispersion Density Imaging (NODDI) is a Watson-distribution based model-dependent technique with metrics of Orientation Distribution Index (ODI) and Neurite Density Index (NDI). The clinical applications of dMRI often rely on such metrics, since it is possible to map diffusion characteristics such as WM complexity, diffusion anisotropy, fibre density, etc. via these metrics. Therefore, these metrics can be considered as biomarkers of neurodegenerative diseases [6, 7, 8, 9].

The main drawback of multi-shell dMRI is the prolonged acquisition time. The reconstruction of these complex metrics require q-space to be sampled extensively. The necessity to include approximately 45 to 200 gradient points increase acquisition times, compared to for example DTI acquisition that only requires 7 measurements. Furthermore, dMRI typically utilizes two acquisitions with identical parameters but in reversed phase encoding (PE) directions for the correction of magnetic susceptibility induced distortions, causing a doubling of the total acquisition time. Accelerating multi-shell dMRI protocols to increase the efficiency

and to exploit the full clinical potential of these techniques is one of the important research topics in the field of dMRI [10, 11, 12, 13]. Most of these techniques focused on sparse q-space measurements and recovering fully sampled dMRI data using various compressed sensing approaches. In addition, several studies investigated the optimal parameters such as the optimal number of q-space points and the optimal b-value range for multi-shell dMRI techniques [14, 15].

In this thesis, 20 different undersampling strategies categorized under 3 different approaches are proposed for accelerating multi-shell HARDI protocols. The performances of these strategies are assessed at acceleration rates of R=2 and R=3. The accuracy of the estimated dMRI metrics for DTI, MSMT-CSD, and NODDI models, together with the accuracy of the diffusion orientation distributions, are assessed in detail using both qualitative and quantitative analyses. The results of this thesis will benefit clinical studies to design accelerated multi-shell HARDI protocols targeting a specific metric and/or a specific disease, with the goal of minimizing the total acquisition time while preserving the maximum amount of information.

Chapter 2

Background and Theory

2.1 Diffusion Principles and Diffusion MRI

Diffusion Magnetic Resonance Imaging is a non-invasive imaging modality based on measuring random movement of water molecules within the targeted tissues. The water molecules diffuse in a fluid following a Brownian motion, which can be described as a random motion whose characteristics depend on the enclosed space. This random motion is referred to as diffusion, which is observed as isotropic in a free environment and anisotropic in a hindered or restricted space. In tissue, especially in the brain where diffusion is often measured, the white matter and gray matter fiber bundles and neurite structures bound the environment. The diffusion occurring in intra-neurite compartments, called restricted diffusion, or in extra-neurite compartments, called hindered diffusion, are both examples of anisotropic diffusion. By measuring the anisotropic diffusion, it is possible to reveal important information about the microstructure of the tissue. [16, 4].

Measuring the movement of water molecules within the neurite tissues allows us to reveal the orientation of axons and map the diffusion anisotropy by Diffusion Weighted Imaging (DWI). [16]

4

2.1.1   Diffusion Magnetic Resonance Imaging

The water molecules in neurite tissue, i.e., in white matter and gray matter fiber bundles, follow Brownian motion. This motion causes additional spin dephasing during magnetic field gradients, which essentially leads to signal attenuation and can be detected with MRI sequences sensitized to diffusion.
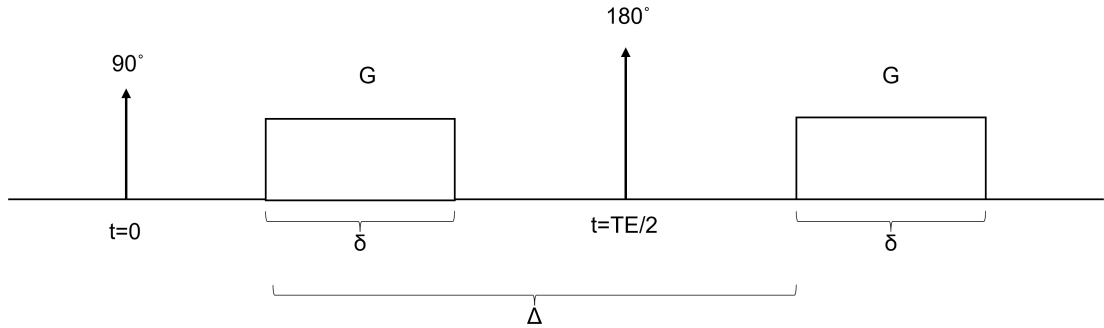
Figure 2.1: *The spin-echo diffusion MRI sequence. This sequence incorporates two diffusion-sensitizing gradient pulses, one before and one after the 180° refocusing RF pulse.*

One of the first and most frequently used diffusion sensitizing pulse sequences is a manipulated spin-echo sequence. As shown in Figure 2.1, this sequence basically incorporates two gradient pulses, one before and one after the 180° refocusing RF pulse. These gradient pulses typically have large gradient amplitudes, long pulse durations, and long separation time (also known as diffusion time). It is possible to measure diffusion along a targeted direction by adjusting the applied gradient direction. The diffusion "sensitivity" of the gradients can be altered by changing the magnitude or the pulse duration, creating a contrast mechanism that allows one to measure the Apparent Diffusion Coefficient (ADC) of different tissues.

Here, as shown in Figure 2.1 assume a randomly moving spin with time-varying position $x(t)$, which experiences a total magnetic field of a combination of a stationary field B_0 and a time-varying diffusion-sensitizing gradient of amplitude $G(t)$ for a period of time τ. Then, the acquired phase would be [1]:

$$\phi(\tau) = -\gamma(B_0 \ + \int_0^\tau G(t)x(t)dt) \tag{2.1}$$

5

Here, γ is the gyromagnetic ratio. Now assume that the first diffusion-sensitizing gradient has a pulse duration of δ and a constant amplitude of G, and the spin is at a constant position x_1 throughout this gradient pulse. Then, considering the phase negating effect of the 180° refocusing RF pulse, the phase shift would be:

$$\phi_1 = \gamma(B_0 + Gx_1)\delta \tag{2.2}$$

Next, assume that the spin moved to the position x_2 during the diffusion time Δ and stayed at that position afterwards. Applying the second diffusion-sensitizing gradient with a matching amplitude G and pulse duration δ, the acquired phase shift would be:

$$\phi_2 = -\gamma(B_0 + Gx_2)\delta \tag{2.3}$$

Then, at the echo time (TE) the net phase shift would be [1]:

$$\phi_{net} = \phi_1 + \phi_2 = -\gamma(x_2 - x_1)\delta \tag{2.4}$$

During the diffusion process, since all spins move randomly, there is always a net phase shift. For an ensemble of spins, the random phase dispersion causes the measured diffusion signal to be attenuated, which is an essential phenomenon in diffusion MRI [1, 4].

The signal in diffusion MRI can be expressed, in the most simplistic sense, as follows:

$$S(b) = S_0 e^{-bD} \tag{2.5}$$

Here, $S_0 = S(b = 0)$ is the non-diffusion weighted signal, D is the ADC with a unit of mm^2/s, and b is the b-value with a unit of s/mm^2. The b-value depends on the pulse duration, diffusion time, and gradient amplitude, which are used to tune signal attenuation:

$$b = q^2(\Delta - \delta/3) \tag{2.6}$$

$$q = \gamma \Delta G \tag{2.7}$$

Here, q is called the wavevector. By adjusting the gradients one can navigate and encode the q-space, which can be defined as the diffusion space where we can measure the diffusion signal attenuation. By changing the b-value, the dephasing

caused by the gradients can be adjusted, which is essential for dMRI of different body parts such as brain, spine, and prostate [4]. It is possible to represent dMRI signal with both q and b.

ADC can be estimated from Eqn. 2.5 by acquiring a single diffusion-weighted and a single non-diffusion weighted (i.e., b0) measurement. Note that Eqn. 2.5 does not consider the orientation dependence of the diffusion process and is only valid in the case of free (i.e., isotropic) diffusion. Thus, to measure diffusion in the neurite tissue, where water molecules move inside of naturally bounded fibers, this signal model is not sufficient.

2.1.2 Diffusion Tensor Imaging

One of the most popular techniques to model diffusion anisotropy is Diffusion Tensor Imaging (DTI), which requires 6 q-space measurements and 1 non-diffusion weighted measurement. Since the diffusion phenomenon is assumed to be symmetric, the diffusion tensor is represented as a positive definite and symmetric tensor as follows:

$$\mathbf{D} = \begin{bmatrix} D_{xx} & D_{xy} & D_{xz} \\ D_{xy} & D_{yy} & D_{yz} \\ D_{xz} & D_{yz} & D_{zz} \end{bmatrix} \tag{2.8}$$

The eigenvectors and eigenvalues of this tensor are used to construct an ellipsoid as shown in Figure 2.2(a), which represents the anisotropic diffusion. More specifically, the eigenvectors $(\mathbf{e_1}, \mathbf{e_2}, \mathbf{e_3})$ determine the orientation of the main axes of the ellipsoid. In addition, the eigenvalues $(\lambda_1, \lambda_2, \lambda_3)$ represent the diffusion displacements along the three orthogonal directions $(\mathbf{e_1}, \mathbf{e_2}, \mathbf{e_3})$ and also determine the length of the principle axes of the diffusion ellipsoid. The eigenvector with the largest eigenvalue corresponds to the primary fiber orientation. Using the diffusion tensor, the anisotropic diffusion can be expressed as an extension of Eqn. 2.5 as follows [4]:

$$S(\mathbf{g}, b) = S_0 e^{-b\mathbf{g}^T \mathbf{D} \mathbf{g}} \tag{2.9}$$

Here, $\mathbf{g} = \mathbf{q}/|\mathbf{q}|$ is a unit vector that encodes the gradient direction.

Important metrics can be derived from the diffusion tensor, which are utilized in the analysis of diffusion and used frequently in clinical applications for the diagnosis of several neuro-degenerative diseases. One of the most important metrics characterizing the diffusion tensor is Fractional Anisotropy (FA), which is a measure of diffusion anisotropy of the tissue:

$$FA = \frac{\sqrt{(\lambda_1 - \lambda_2)^2 + (\lambda_2 - \lambda_3)^2 + (\lambda_3 - \lambda_1)^2}}{\sqrt{2}\sqrt{\lambda_1^2 + \lambda_2^2 + \lambda_3)^2}} \tag{2.10}$$

$$0 \leq FA \leq 1 \tag{2.11}$$

Another important metric, Mean Diffusivity (MD), maps the average diffusion in the orientation of the three eigenvectors in each voxel:

$$MD = \frac{\lambda_1 + \lambda_2 + \lambda_3}{3} \tag{2.12}$$
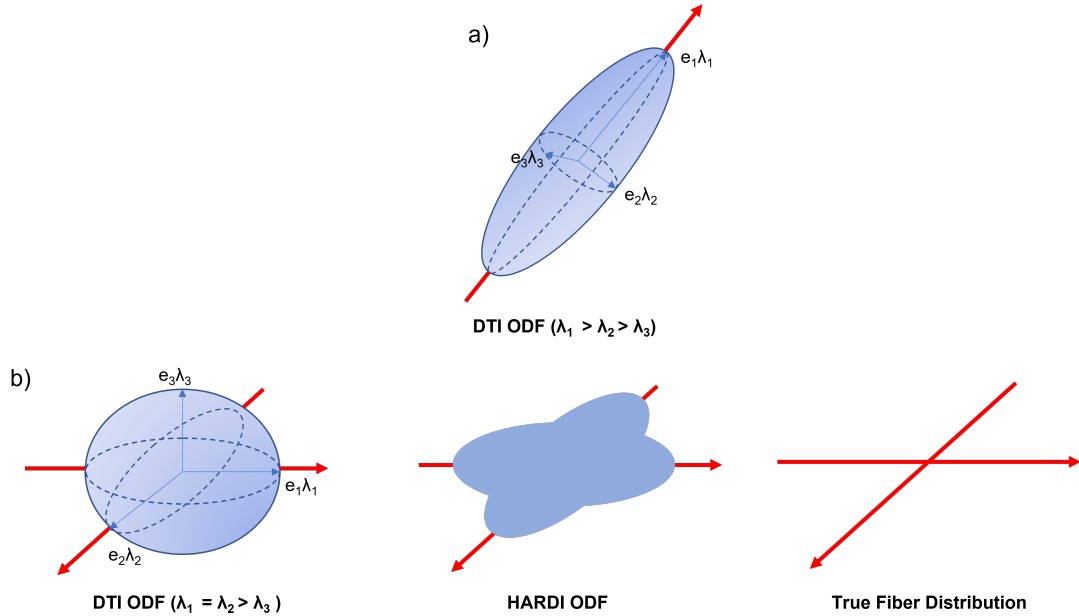
Figure 2.2: *(a) DTI can resolve only the primary fiber orientation. The largest eigenvalue determines the primary fiber orientation in a voxel and can be represented by an ellipsoid with non-uniform primary axes. (b) When crossing fibers problem is observed with voxels containing complex fiber structures, DTI fails to resolve the true fiber distrubution, with $\lambda_1 = \lambda_2$. However, HARDI techniques can estimate ODF coefficients, whose maximas are aligned with the true fiber distribution.*

2.1.3 Crossing Fibers Problem

DTI can only resolve a single fiber orientation, assuming simple unidirectional fiber structures exist in each voxel. For example, as shown in Figure 2.2(b), $\lambda_1 = \lambda_2$ would correspond to an ellipsoid with two axes of equal length, making it impossible to resolve the true fiber orientation. Often, there exists more than one fiber bundle organization in each voxel. Especially in brain tissue consisting of very complex fiber structures, fibers are often crossing, fanning or tangent to each other [16]. To resolve such complex structures, more advanced diffusion MRI techniques are required.

2.2 High Angular Resolution Diffusion Imaging

High Angular Resolution Diffusion Imaging (HARDI) further extends DWI by sampling the q-space as extensively as possible, with many gradient directions and b-values [2]. The diffusion data is then used to estimate the true diffusion distribution by reconstructing the Orientation Distribution Function (ODF), which is the diffusion Probability Density Function (PDF). Here, instead of the MRI signal, the signal attenuation $E(\mathbf{q}, t) = S(\mathbf{q}, t)/S_0$ is considered as follows:

$$E(\mathbf{q}, t) = \int_{R^3} p(\mathbf{r}, t) e^{-2\pi i \mathbf{q}^T \mathbf{r}} d\mathbf{r} = \mathcal{F}\{p(\mathbf{r}, t)\} \tag{2.13}$$

Here, $p(\mathbf{r}, t)$ is the diffusion propagator function, which measures the probability of observing the diffusing particle at location $\mathbf{r}$ after a diffusion time t. This function is modeled as a Gaussian in the case of isotropic diffusion [4]. In this equation, $\mathcal{F}(\cdot)$ denotes the Fourier Transformation (FT) relationship between the signal attenuation in q-space and the diffusion propagator. Therefore, exploiting this relationship, the diffusion propagator can be reconstructed by taking the inverse FT of the signal attenuation with respect to $\mathbf{q}$ [4]:

$$p(\mathbf{r}, t) = \mathcal{F}^{-1}\{E(\mathbf{q}, t)\} \tag{2.14}$$

Note that the FT relationship would require sampling of the whole q-space to reconstruct the true propagator, which is practically impossible. Therefore, in

many reconstruction techniques, the ensemble average propagator (EAP) is considered instead of the true propagator.

ODF can be defined from the EAP, and captures the complete angular content of the true diffusion propagator: [2]:

$$\Psi(\theta, \phi) = \int_0^\infty p(r, \theta, \phi) r^2 dr \tag{2.15}$$

Here, $p(r, \theta, \phi)$ is the diffusion propagator expressed in spherical coordinates, with $\theta \in [0, \pi]$ and $\phi \in [0, 2\pi]$. ODF succesfully captures the angular information of HARDI signal and diffusion propagator. The peaks of the ODF are aligned with the underlying true fiber distribution, allowing many metrics and advanced visualization approaches to be implemented [4].

There are two main HARDI strategies. The first one is sampling the q-space using a Cartesian grid as densely as possible, which is generally associated with Diffusion Spectrum Imaging (DSI) [17, 4]. DSI requires a large number of samples (N), typically greater than 200, to be collected for the reconstruction of the diffusion propagator to be accurate. Another method is to sampling the q-space on a single spherical surface whose radius is determined by the b-value, which is called Single-Shell HARDI.

2.2.1   Single-Shell HARDI

Single-Shell HARDI is a convenient diffusion imaging technique that allows us to exploit the angular information of the diffusion propagator. Compared to DSI, single-shell HARDI is operational with fewer samples of approximately N=60 [2]. It is possible to increase the accuracy of ODF estimation by increasing the density of the sampling pattern.
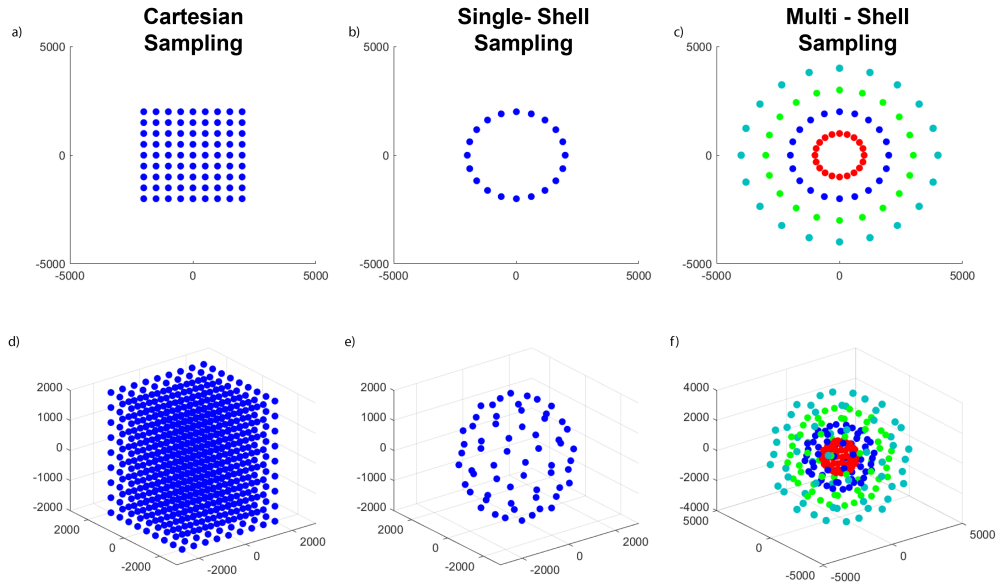
Figure 2.3: *Different sampling approaches for HARDI acquisitions. (a,d) DSI samples the q-space in a Cartesian grid, typically consisting of more than 200 samples for extensive coverage. (b,e) Single-shell HARDI samples the q-space on a single spherical surface whose radius is determined by the b-value. This sampling provides high angular resolutions, with fewer measurements compared to DSI. HARDI aims to reconstruct an ODF that captures the angular information of the diffusion signal and its maxima are aligned with the underlying true fiber distributions. (c,f) Multi-shell HARDI extends the spherical sampling idea to multiple spherical surfaces with radii determined by b-values. This sampling allows one to benefit both from the high angular resolution of the high b-value acquisitions and high SNR of the low b-value acquisitions.*

2.2.2 Spherical Harmonic Decomposition

Spherical Harmonics (SH) are complex-valued functions that satisfy the Laplace's equation in sphrecial coordinates. Importantly, they can be used as orthonormal basis functions for complex spherical functions defined on the unit sphere [4]. Here, sampled on a sphere with a fixed radius, single-shell HARDI signal is a complex spherical function that we can decompose using SH basis functions. The HARDI signal $\mathbf{S}$ is measured in each voxel for each one of the N diffusion-weighted gradient directions of the gradient table: $\mathbf{S} = \{S(\mathbf{g_1}) \cdots S(\mathbf{g_N})\}$. Assuming that the HARDI signal is real and symmetric (since the diffusion is also symmetric), only SHs of even orders (i.e., antipodally symmetric SHs) are utilised in the

expansion [2].

In order to perform SH decomposition on the HARDI signal directly, it is necessary to formulate real and symmetric SH basis functions [2]:

$$
Y_j = \begin{cases}
\sqrt{2}\, Re(Y_l^{|m|}), & \text{if } m \leq 0 \\
Y_l^m, & \text{if } m = 0 \\
\sqrt{2}(-1)^{m+1}\, Im(Y_l^m), & \text{if } m > 0.
\end{cases} \tag{2.16}
$$

Here, $Y_l^m(\theta, \phi)$ is the SH of the order l and degree m, with $m = -l, ..., 0, ..., l$ and $l = 0, 2, 4, ..., L$, a new index $j(l, m) = (l^2 + l + 2)/2 + m$ is defined. Accordingly, Y_j forms an orthonormal real and symmetric basis for the HARDI signal attenuation, which can be directly represented with a weighted superposition of SHs:

$$
S(\theta_i, \phi_i) = \sum_{j=1}^{R} c_j Y_j(\theta_i, \phi_i) \tag{2.17}
$$

Here, $S(\theta_i, \phi_i)$ is the HARDI signal in diffusion-weighted gradient direction i, and c_j is the SH coefficient, and Y_j is the symmetric and orthonormal SH basis functions of order j. In addition, R is the number of terms in the SH decomposition.

2.2.3   Spherical Deconvolution

The measured MRI signal can be defined as the convolution of the actual image with the imaging point spread function, i.e., the impulse response function. Similarly applied to HARDI, the signal measured on a single-shell in q-space can be expressed as the spherical convolution of the true fiber distribution of the underlying tissue in a voxel and the "impulse response function" corresponding to the single fiber response.

Assuming that all fiber bundles in the brain share the same diffusion characteristics, together with some additional set of assumptions, the signal attenuation measured from the voxels containing only a single coherent fiber population oriented in a specific direction would be identical except for their orientations. Therefore, they can be expressed using a single fiber response function, $R(\theta)$ [18].

Then, by rotating the single fiber response to reflect the desired orientation and weighting it with the accurate volume fraction for that fiber bundle, the HARDI signal $S(\theta, \phi)$ can be represented as a weighted superposition of single fiber responses. This operation corresponds to a convolution of the single fiber response $R(\theta)$ and fiber-ODF (fODF), $F(\theta, \phi)$, as follows:

$$F(\theta, \phi) = \sum_{i=1}^{N} v_i \delta(\theta_i, \phi_i) \tag{2.18}$$

$$S(\theta, \phi) = F(\theta, \phi) \bigotimes R(\theta) \tag{2.19}$$

Here, $F(\theta, \phi)$ incorporates the volume fractions of the fibers in the voxel aligned along the direction (θ, ϕ). v_i is the fiber volume fraction, N is the number of distinct fibers (i.e., the number of volume fractions within the voxel), and $\delta(\theta, \phi)$ is the dirac delta function along the direction (θ, ϕ). Typically, the voxels with an FA greater than 0.7 are used to estimate the single fiber response function.

Given the underlying convolution relation in Eqn. 2.19, the fODF can be reconstructed by a spherical deconvolution (SD) operation. Here, the SH basis introduced in Section 2.2.2 becomes really useful. Firstly, for the lth order SH representation, Eqn. 2.19 can be rewritten in matrix form as follows:

$$\mathbf{s_l} = \mathbf{R_l} \mathbf{f_l} \tag{2.20}$$

Here, the vectors $\mathbf{s_l}$ and $\mathbf{f_l}$ are the lth order SH space representation of $S(\theta, \phi)$ and $F(\theta, \phi)$, respectively. Likewise, the matrix $\mathbf{R_l}$ is the lth order SH representation of the response function $R(\theta)$. Using this matrix relation, f_l can be obtained by SD, which now corresponds to a simple matrix inversion. It is possible to solve this problem by a linear least squares formulation. However, this problem is ill-posed, and especially for the higher harmonic orders, the solution is unstable [5].

2.2.4   Constrained Spherical Deconvolution

In order to overcome the limitations of SD and prevent negative fODF estimations, a positivity constraint is introduced to the problem, leading to a robust

fODF estimation. The approach here is to penalize the negative fODF values after a preliminary estimation of fODF coeficients are made. Then, the constraint is enforced as a Tikhonov regularization and the fODF coefficients can be estimated by iteratively solving the following equation [5]:

$$\hat{\mathbf{f}} = \arg \min_{\mathbf{f}} \frac{1}{2} ||\mathbf{C}\mathbf{f} - \mathbf{s}||^2 \qquad \text{subject to } \mathbf{L}\mathbf{f} \geq 0 \qquad (2.21)$$

Here, $\mathbf{f}$ is the fODF coefficients to be estimated, $\mathbf{s}$ is the measured signal intensity, $\mathbf{C}$ is the spherical convolution kernel, and $\mathbf{L}$ is the constraint matrix.

One of the main metrics of this Constrained Spherical Deconvolution (CSD) is Apparent Fiber Density (AFD), which is useful for investigating both the performance of the reconstruction and the possible pathologies altering the diffusion characteristics of the tissue. AFD is simply defined as the magnitude of fODF. Another main metric is number of Fiber Orientations (nuFO), which is computed as the number of maximas (or peaks) of the fODF. Because each maxima of the fODF is associated with a potential fiber along the corresponding direction, nuFO is a measure of the local WM complexity.

2.3 Multi-Shell Diffusion Imaging

Multi-Shell HARDI extends the idea of single-shell HARDI by sampling the q-space on more than one spherical surface, each with a fixed radius determined by the b-value, as densely as possible. This sampling strategy increases angular resolution without losing from the Signal-to-Noise Ratio (SNR). High b-value (e.g., $b \geq 2000 \ s/mm^2$) acquisitions provide high angular resolution at reduced SNR, whereas low b-value (e.g., $b \leq 700 \ s/mm^2$) acquisitions have high SNR with reduced angular resolution. Using a multi-shell sampling strategy increases the ODF estimation accuracy. There exists many methods that utilize multi-shell HARDI signal to reconstruct the underlying fiber distribution, either by estimating the ODF coefficients or the orientation dispersion based on both model-free and model-dependent techniques.

2.3.1 Multi-Shell Multi-Tissue Constrained Spherical Deconvolution

Multi-Shell Multi-Tissue Constrained Spherical Deconvolution (MSMT-CSD) is a model-free technique that further extends the CSD implementation, incorporating the diffusion characteristics of different tissue types and multi-shell q-space data. In the case of the brain, there exist three main tissue types: white matter (WM), grey matter (GM), and cerebrospinal fluid (CSF). The previous implementations of CSD would produce noisy and unstable single fiber response estimations for GM and CSF due to their distinct diffusion characteristics. To overcome this problem, the CSD problem introduced in Eqn. 2.21 can be extended to include n tissue types within a voxel and diffusion data acquired on m shells as follows [19]:

$$
\begin{bmatrix} \hat{\mathbf{f}}_1 \\ \vdots \\ \hat{\mathbf{f}}_n \end{bmatrix} = \arg\min_{\begin{bmatrix} \mathbf{f}_1 \\ \vdots \\ \mathbf{f}_n \end{bmatrix}} \frac{1}{2} \left\| \begin{bmatrix} \mathbf{C}_{1,1} & \cdots & \mathbf{C}_{1,n} \\ \vdots & \ddots & \vdots \\ \mathbf{C}_{m,1} & \cdots & \mathbf{C}_{m,n} \end{bmatrix} \begin{bmatrix} \mathbf{f}_1 \\ \vdots \\ \mathbf{f}_n \end{bmatrix} - \begin{bmatrix} \mathbf{s}_1 \\ \vdots \\ \mathbf{s}_m \end{bmatrix} \right\|_2^2
$$

$$
\text{subject to} \quad \begin{bmatrix} \mathbf{L}_1 & \mathbf{0} & \mathbf{0} \\ \mathbf{0} & \vdots & \mathbf{0} \\ \mathbf{0} & \mathbf{0} & \mathbf{L}_n \end{bmatrix} \begin{bmatrix} \mathbf{f}_1 \\ \vdots \\ \mathbf{f}_n \end{bmatrix} \geq \mathbf{0} \quad (2.22)
$$

Here $\hat{\mathbf{f}}_j$ is the vector of estimated fODF coefficients for the jth tissue, $\mathbf{s}_i$ is the vector of HARDI signals measured on the ith shell, $\mathbf{C}_{i,j}$ is the spherical convolution kernel matrix for the jth tissue on the ith shell, and finally $\mathbf{L}_j$ is the constraint matrix for the jth tissue. Here, WM ODF is assumed to be anisotropic. In contrast, CSF and GM ODFs are assumed to be isotropic, which can be represented with an SH basis of order zero [19]. This technique not only increases the accuracy of ODF estimation of WM fibers, but also allows one to estimate ODFs of GM and CSF volume fractions.

2.3.2 Neurite Orientation Dispersion Density Imaging

Different than CSD techniques, Neurite Orientation Dispersion Density Imaging (NODDI) is a multi-shell HARDI technique that introduces a three compartment tissue model consisting of intra-neurite, extra-neurite, and CSF volume fractions. Here, the orientation-dispersed cylinder model is used to estimate the neurite density and the orientation dispersion in each volume fraction [20]. The tissue model is defined considering distinct diffusion profiles (i.e., restricted, hindered, and isotropic) as follow:

$$A = (1 - \nu_{iso})(\nu_{ic}A_{ic} + (1 - \nu_{ic})A_{ec}) + \nu_{iso}A_{iso} \tag{2.23}$$

In this equation, A_{ic}, A_{ec}, and A_{iso} are the normalized HARDI signals measured in intra-neurite, extra-neurite, and isotropic/CSF compartments, respectively. In addition, ν_{ic} and ν_{iso} are the intra-neurite and isotropic volume fractions, respectively. More specifically, the intra-neurite and extra-neurite signals can be expressed as:

$$A_{ic} = \int f(\mathbf{n})e^{-bd_{||}(\mathbf{q}\cdot\mathbf{n})^2}d\mathbf{n} \tag{2.24}$$

$$\log A_{ec} = -b\mathbf{q}^T \left(\int f(\mathbf{n})D(\mathbf{n})d\mathbf{n} \right) \mathbf{q} \tag{2.25}$$

In these equations, $D(\mathbf{n})$ is the cylindrically symmetric tensor with $\mathbf{n}$ corresponding to its principal direction of diffusion. In addition, $d_{||}$ and $d_\perp$ are the intrinsic diffusivities parallel and perpendicular to the direction $\mathbf{n}$, respectively, and are related by $d_\perp = d_{||}(1 - \nu_{ic})$. Finally, $f(\mathbf{n})$ is the ODF, modeled as a Watson distribution instead of the SH representations introduced in the previous sections. Here, the main goal is to estimate the orientation dispersion (OD) rather than the ODF [20]. Finally, the CSF signal is modeled as isotropic diffusion with a Gaussian distribution.

Orientation Dispersion Index (ODI), which is the primary metric of NODDI, is defined as [20]:

$$ODI = \frac{2}{\pi}arctan\left(\frac{1}{\kappa}\right) \tag{2.26}$$

Here, κ is the concentration parameter of the Watson distribution in the axon-stick model used in NODDI. It measures the orientation dispersion around the

mean orientation of the Watson distribution. Another important metric of NODDI is Neurite Density Index (NDI), which can be mapped with the estimated intra-neurite volume fraction, ν_{ic}.

NODDI fits the model to the HARDI signal through the Gauss-Newton optimization, which determines the Maximum-Likelihood Estimation (MLE) of the parameters. The main aim is to estimate κ, which quantifies the orientation dispersion, as accurately as possible. The model depends on a set of fixed a-priori parameters [20]. NODDI requires a multi-shell HARDI acquisition of at least two shells.

2.4   Multi-Shell Diffusion MRI Metrics

Multi-shell dMRI techniques allow microstructure of the neurite tissue to be resolved with high resolution and high SNR at the same time, which is valuable to map the neurite density, diffusion anisotropy, fiber orientations, and fiber dispersion. These properties are clinically valuable and they are used in the diagnosis of many degenerative diseases. Thus, multi-shell dMRI metrics, derived from the estimated coefficients and visualized as metric maps, can be considered as the most important outputs of the techniques described in the previous sections.

The metrics introduced in the earlier sections can be regrouped as anisotropy indices and fiber density indices. In this thesis, 6 different diffusion metrics are investigated: FA and MD for DTI, AFD and nuFO for MSMT-CSD, and ODI and NDI for NODDI.

As introduced in Section 2.1.2, FA is a measure of diffusion anisotropy and MD is the overall average diffusivity. Although these metrics contains a lot of information about the WM integrity and tissue characteristics, HARDI metrics provide more specific and sensitive analysis. For instance, NDI and ODI are measures for density and orientation dispersion of the fibers. These NODDI metrics resolve two main components of FA, allowing more in depth analysis of

anisotropy observed through fiber bundles [20]. Similarly, AFD highlights the fiber density per unit volume and is a more biologically specific and accurate metric, especially in voxels containing crossing fibers. AFD is proportional to the intra-neurite volume fraction and can be computed for each fiber bundle separately [19]. In addition, nuFO is the number of fODF maxima in a voxel, and is used as a metric to measure the local WM complexity. Similar to the NODDI metrics, these MSMT-CSD metrics also provide an in depth analysis of the tissue, allowing one to investigate the components contributing to diffusion characteristics separately.

The most valuable aspect of these dMRI metrics is their suitability for being used as biomarkers for neurodegenerative diseases. For the diagnosis of temporal lobe epilepsy AFD changes becomes a diagnostic tool [8], while the low intensity patches in NDI maps are used to ease diagnosis of focal cortical dysplasia [21]. NODDI metrics ODI and NDI can be further used to detect glioma [22], and a decrease in NDI was observed in the WM tissue of tuberculosis sclerosis patients [23]. Increased MD and decreased FA were reported for Alzherimer's Disease patients in several studies [24, 25].

Although multi-shell dMRI metrics are valuable in the diagnosis of neurodegenerative diseases and provide information at an increased resolution compared to DTI metrics (especially in the voxels with multiple fiber orientations and complex fiber structures), they come with a major disadvantage of prolonged acquisition times. Both NODDI and MSMT-CSD methods require multi-shell HARDI data to be collected, whose protocols have an acquisition time of approximately 30 minutes. These long acquisition times are especially problematic for the patients with neurological diseases such as epilepsy, Multiple Sclerosis (MS), Alzheimer's Disease, etc. Therefore, shortening the acquisition time of multi-shell dMRI acquisitions becomes vital and is an active area of research [10, 11].

Chapter 3

Methods

This chapter is based in parts on the following publications:

- Aygun E, Saritas EU. Performance Analysis of Undersampling Strategies for Multi-Shell Diffusion MRI. In the Proceedings of the 30th Annual Meeting of ISMRM, London, United Kingdom, 2022.

- Aygun E, Saritas EU. Comparison of Diffusion Metrics under Different Undersampling Strategies for Multi-Shell Diffusion MRI. 2021 Medical Technologies Congress (TIPTEKNO), 2021, pp. 1-4, DOI: 10.1109/TIPTEKNO53239.2021.9632947.

3.1   Dataset

The undersampling strategies for multi-shell dMRI were evaluated using the Human Connectome Project (HCP) 1200 Subjects Data release [26]. For this evaluation, 20 healthy subjects were chosen randomly. HCP multi-shell dMRI data was acquired with a multi-band multi-shell diffusion protocol on a 3 T Siemens scanner, using a spin-echo echo planar imaging (EPI) sequence. The diffusion gradient table consists of 6 non-diffusion weighted volumes (i.e, $b=0$ s/mm^2) and

3-shells of $b=1000$, $b=2000$, and $b=3000$ s/mm^2 with 30, 29, and 30 gradients directions, respectively. The resulting multi-shell q-space sampling scheme has 89 b-vectors, which are displayed in Figure 3.1(a). Other imaging parameters were: FOV = 210×180 mm, 1.25 mm isotropic resolution, TR/TE= 5520/89.5 ms. The total acquisition time was approximately 20 minutes.

Diffusion MRI images suffer from the magnetic susceptibility induced artifacts that highly affect both visual and quantitative quality of the diffusion metrics. To overcome this problem, the HCP dataset contains 2 volumes acquired with the same diffusion gradient table and imaging parameters, albeit with reversed PE directions of Right-to-Left (RL) and Left-to-Right (LR). Susceptibility induced distortions occur along the PE direction of the EPI images. Therefore, the reversed PE acquisitions experience distortions in opposite directions, which can be observed in the example images shown in Figure 3.3(a-b). These acquisitions can then be utilized to estimate the susceptibility induced off-resonance field map and correct the susceptibility induced artifacts using FSL TOPUP [27], [28].

3.2 Undersampling Strategies

To investigate the effects of decreasing the total acquisition time of HARDI protocols on the multi-shell diffusion MRI metrics, we designed different q-space undersampling strategies for acceleration rates of R=2 and R=3. The strategies incorporate the effects of choosing different number of gradient directions per shell, different number of shells, and different susceptibility artifact correction techniques. To this end, by undersampling the original q-space data, 10 different undersampling strategies were designed and applied for both R=2 and R=3, creating a unique gradient table for each case. Independent from the acceleration rate and the strategy, q-space was undersampled based on electrostatic repulsion algorithm [29]. For this purpose, Camino *subsetpoints* tool was utilized to undersample the q-space points on each shell separately, using the Electrostatic Energy Minimization (EEM) technique [30].

The strategies for R=2 decreased the total acquisition time to approximately 10 minutes. The 10 gradient schemes applied for this case, together with the reference fully-sampled HCP diffusion gradient table properties, can be seen in Figure 3.1. Here, the first 9 strategies depend on undersampling the q-space points, i.e., decreasing the total number of b-vectors to 45. The last strategy reduces the acquisition time by acquiring reversed PE images for a single b0 volume only. Overall, these strategies can be grouped under 3 different categories:

- **3-shell Strategies:** All 3-shell gradient schemes contained 45 b-vectors distributed over 3 shells with b=1000, 2000, and 3000 s/mm^2 at different rates. Six different strategies were considered. In the first strategy titled "3-13-29", the b-vectors were distributed in proportion with the surface area of each shell, so that the b-vector density was approximately the same on all shells. For the strategies titled "5-15-25" and "10-15-20", the density of the b-vectors was increased gradually for the lower shells. Each shell was undersampled so that the difference between the number of b-vectors of consecutive shells was 10 and 5 for "5-15-25" and "10-15-20", respectively. The strategies titled "5-20-20" and "10-10-25" were modified versions of the previous two strategies, such that they have the same number of b-vectors on either the last two or the first two shells. A scheme with 15 b-vectors in each shell, labeled as "15-15-15", was also included to compare the effect of uniform vs. non-uniform b-vector distributions.

- **2-shell Strategies:** All 2-shell schemes contained 45 b-vectors distributed over b=1000 and 2000 s/mm^2 shells. Here, the first two shells were chosen to maintain high SNR in the measurements. Three different schemes were considered. The gradient scheme titled "22-23" distributed the b-vectors as close to uniformly as possible, while "16-29" and "30-15" fully preserved the second and first shell while undersampling the first and second shell, respectively.

- **Single b0 TOPUP:** All of the aforementioned strategies focus on undersampling the b-vectors directly, and apply the same susceptibility correction technique based on reversed PE images (see Section 3.3 for details).

However, the process of acquiring images in reversed PE directions doubles the total acquisition time of the HARDI protocols. Eliminating all volumes acquired in the reversed PE direction would effectively accelerate the multi-shell HARDI protocol. Here, instead of acquiring reversed PE directions for every b-vector, the reversed PE directions are acquired for a single b0 volume only, whereas the diffusion-weighted volumes are acquired fully but with a single PE direction. This scheme effectively applies an acceleration of R=2, while preserving the original diffusion gradient table with 89 b-vectors. In this case, the distortion correction needs to be applied differently, using Jacobian modulation technique of TOPUP (see Section 3.3 for details). Since HCP dataset contains 6 b0 volumes acquired in reversed PE directions, we separated one of the b0 volumes from the LR acquisition to be used as the only opposing PE b0 volume.

Similar to the R=2 case, we also created diffusion gradient tables for an acceleration rate of R=3 to apply similar undersampling strategies, which are shown in Figure 3.2. Again, these strategies can be grouped under 3 different categories:

- **3-shell Strategies:** There are 6 undersampling strategies under this group, which are adapted from the 3-shell strategies presented for the R=2 case. These strategies reduce the total acqustion time to one-third by under-sampling the q-space data with EEM technique, and contain 30 b-vectors distributed over 3 diffusion shells. The first strategy titled "2-9-19" under-samples b-vectors in proportion to the surface areas of the shells. "5-10-15" and "7-10-13" strategies gradually increase the b-vector density over the lower shells, and have a difference in b-vectors of 5 and 3 between two consecutive shells, respectively. The strategies titled "5-12-13" and "7-7-16" are modified versions of the previous two strategies, such that they sample either the last two or the first two shells uniformly (or approximately uniformly). Finally, the strategy labeled as "10-10-10" uniformly samples all 3 shells.

- **2-shell Strategies:** These strategies contain 30 b-vectors distributed over

the first 2-shells, b=1000 and 2000 s/mm^2. The strategy labeled as "15-15" uniformly distributes the b-vectors. The strategies titled "10-20" and "20-10" perform non-uniform undersampling and distribute the b-vectors in proportion and in inverse proportion to the b-values of the two shells.

- **Single b0 TOPUP:** The main idea in this strategy is to not undersample the b-vectors, but to eliminate the reversed PE acquisitions for diffusion-weighted volumes. To adapt this idea to the R=3 case, the total number of b-vectors should be 60, i.e., twice the number of b-vectors when compared to 3-shell and 2-shell schemes. Here, we preserved the first two shells to maintain high SNR, and removed the b=3000 s/mm^2 shell entirely. Then, a single reversed PE b0 volume is acquired, and the distortion correction is applied using Jacobian modulation. This scheme effectively reduces the total acqusision time to one-third.

Two-shell and 3-shell undersampling strategies fully preserved the original 6 b0 volumes presented in the reference, fully sampled HCP data. "Single b0 TOPUP" strategy preserved the 6 b0 volumes for one of the PE directions, and acquired a single b0 volume from the opposing PE direction.

3.3   Data Preprocessing

As the first preprocessing step, the susceptibility artifacts in the images were corrected using FSL TOPUP [27], [28]. An example case is shown in Figure 3.3. First, the reversed PE b0 images as shown in Figure 3.3(a,e) were separated from the diffusion-weighted volumes. Then, TOPUP was used to generate off-resonance field map using the b0 volumes acquired in RL (blip-up) and LR (blip-down) PE directions. The pair of diffusion volumes were corrected using the Least-Squares-Restoration (LSR) method of TOPUP using the estimated field coefficients (see Figure 3.3(b-c)), and the output was used in the analysis. This approach was the default distortion correction technique used in this thesis for 3-shell and 2-shell undersampling strategies. For the "Single b0 TOPUP" scheme,

on the other hand, Jacobian modulation method of TOPUP was applied to resample the distorted RL (blip-up) image to the undistorted space (see Figure 3.3(f-g)). Here, only a single pair of b0 volumes were acquired in reversed PE directions to estimate the off-resonance field map. Then, the distortions in the RL (blip-up) volume were corrected using Jacobian modulation.

As shown in Figure 3.4(a-b), to increase the accuracy of the quantitative quality assessments for DTI, NODDI, and MSMT-CSD metrics, the background noise and non-brain voxels were removed with a binary mask generated with FSL BET tool, using the distortion-corrected image [31]. To improve the MSMT-CSD and DTI analyses, Marchenko-Pastur principal component analysis was applied to the undersampled multi-shell dMRI data for denoising [32] using the DiPY toolbox [33]. CSF is typically not the tissue of interest in dMRI studies [34]. Therefore, as shown in Figure 3.4(c-d), CSF regions were suppressed to assess the effects of undersampling on WM and GM regions. For this purpose, tissue segmentation masks for WM, GM, and CSF volume fractions were generated with FSL FAST and used to conduct quantitative analysis on WM and GM regions only [35].

3.4 Quality Assessment of Multi-Shell Diffusion Metrics

The performance of the proposed undersampling strategies were compared for several multi-shell dMRI methods. DTI, MSMT-CSD, and NODDI were used to extract diffusion orientation information and estimate ODF coefficients for each undersampled gradient scheme, which were then utilized in diffusion metric calculations. Both qualitative and quantitative analyses were performed on the metric maps and ODF coefficients (for DTI and MSMT-CSD). DTI and MSMT-CSD analyses were completed using the DiPY toolbox, where AFD and nuFO maps were retrieved from MSMT-CSD ODF coeffients and FA and MD were computed from the diffusion tensor [33]. For MSMT-CSD, a SH basis of order 8 was utilized. The single fiber response estimation was performed for three tissue

compartments, using voxels with FA > 0.7 for WM and FA> 0.3 for GM regions. ODF of MSMT-CSD was estimated with a relative peak threshold chosen as the half of the maximum peak amplitude in a voxel and the number of maximum peaks were set to 5. Both DTI and MSMT-CSD ODFs were computed on a sphere with 724 fixed directions, independent of the undersampling technique. ODI and NDI were obtained for NODDI analysis, computed using the AMICO toolbox [36] with the parameters as given in [20].

For each undersampling strategy and for every metric, a map was generated for visual inspection. As shown in Figure 3.4, the background voxels, non-brain voxels, and CSF regions were masked out. Then, Structural Smilarity Index Measure (SSIM) [37] and Peak Signal-to-Noise Ratio (PSNR) were computed for quantitative quality assessments. PSNR can be expressed as follows:

$$PSNR = 10 \log_{10} \left(\frac{max(I_{und})^2}{MSE(I_{und}, I_{ref})} \right) \tag{3.1}$$

$$MSE(I_{und}, I_{ref}) = \frac{1}{NM} \sum_{N,M} (I_{ref}(n,m) - I_{und}(n,m))^2 \tag{3.2}$$

Here, I_{und} and I_{ref} are undersampled and reference maps of sizes N×M, respectively.

Additionally, to further assess the performance of the undersampling strategies for MSMT-CSD and DTI, the ODFs estimated for undersampled and fully sampled cases were compared using the Jensen Shannon Distance (JSD). JSD is a metric that measures the similarity between two PDFs defined on the same space and can be expressed as follows [38]:

$$JSD(P|Q) = \sqrt{H(\frac{(P+Q)}{2}) - \frac{H(P) + H(Q)}{2}} \tag{3.3}$$

$$H(X) = - \sum_{x \in X} P(x) \log_2(P(x)) \tag{3.4}$$

Here, P and Q represent the ODFs reconstructed for reference and undersampled cases, respectively. Note that the ODF coefficients estimated given a fixed set of directions on a sphere represent the diffusion PDF. In this thesis, independent of the undersampling approach, the ODF coefficients were estimated on a sphere

with 724 fixed directions. For each direction on the sphere, the corresponding ODF coefficient quantifies the probability of a fiber existing along that direction.
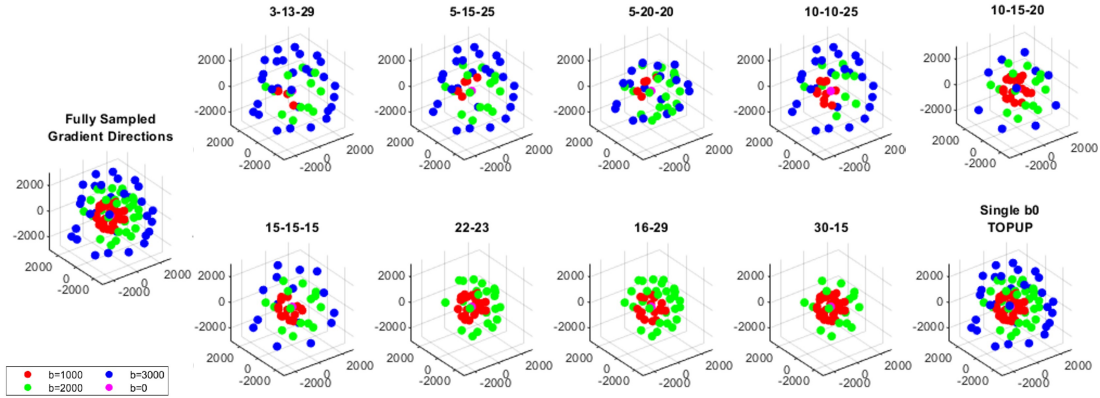
(a) Reference Fully Sampled Scheme and Undersampled Gradient Schemes for R=2

	Ref.	3-13-29	5-15-25	5-20-20	10-10-25	10-15-20	15-15-15	22-23	16-29	30-15	Single b0 TOPUP
No. of Shells	3	3	3	3	3	3	3	2	2	2	3
b-values	1000 2000 3000	1000 2000 3000	1000 2000 3000	1000 2000 3000	1000 2000 3000	1000 2000 3000	1000 2000 3000	1000 2000	1000 2000	1000 2000	1000 2000 3000
No. of b-vectors	30, 29, 30	3, 13, 29	5, 15, 25	5, 20, 20	10, 10, 25	10, 15, 20	15, 15, 15	22, 23	16,29	30,15	30, 29,30
Reverse P.E.	b0 + all	b0 + all	b0 + all	b0 + all	b0 + all	b0 + all	b0 + all	b0 + all	b0 + all	b0 + all	b0

(b) Gradient Table Parameters for R=2

Figure 3.1: *(a) The undersampled gradient schemes in q-space for the acceleration rate of R=2. The reference fully sampled scheme has 89 diffusion-weighted and 6 b0 acquisitions. The first nine undersampling strategies are obtained by applying EEM algorithm to the gradient points of each diffusion shell separately to decrease the number of b-vectors to 45. The last undersampling strategy labeled "Single b0 TOPUP" uses identical b-vectors as the reference. (b) The diffusion parameters and distribution of b-vectors on each shell. For the first nine undersampling strategies, 45 gradient points are either distributed on 3 or 2 shells. The last gradient scheme preserves all 89 b-vectors, but the reversed PE directions are acquired for a single b0 volume only.*
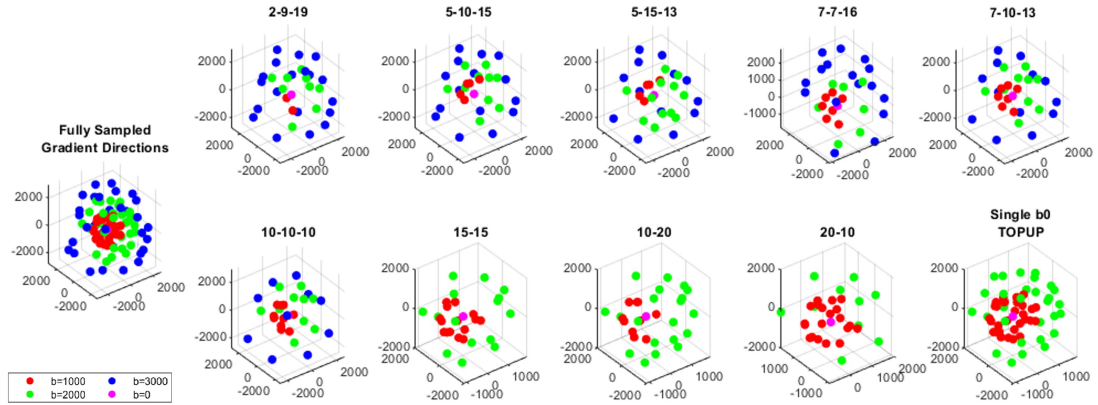
(a) Reference Fully Sampled Scheme and Undersampled Gradient Schemes for R=3

	Ref.	2-9-19	5-10-15	5-12-13	7-7-16	7-10-13	10-10-10	15-15	10-20	20-10	Single b0 TOPUP
No. of Shells	3	3	3	3	3	3	3	2	2	2	2
b-values	1000 2000 3000	1000 2000 3000	1000 2000 3000	1000 2000 3000	1000 2000 3000	1000 2000 3000	1000 2000 3000	1000 2000	1000 2000	1000 2000	1000 2000
No. of b-vectors	30, 29, 30	2, 9, 19	5, 10, 15	5, 12, 13	7, 7, 16	7, 10, 13	10, 10, 10	15, 15	10,20	20,10	30,29
Reverse P.E.	b0 + all	b0 + all	b0 + all	b0 + all	b0 + all	b0 + all	b0 + all	b0 + all	b0 + all	b0 + all	b0

(b) Gradient Table Parameters for R=3

Figure 3.2: *(a) The undersampled gradient schemes in q-space or the acceleration rate of R=3. The reference fully sampled scheme has 89 diffusion-weighted and 6 b0 acquisitions. The 3-shell and 2-shell strategies are obtained by direct undersampling of q-space data using EEM technique applied to each diffusion shell separately. The scheme labeled "Single b0 TOPUP" is obtained by applying discarding the 3rd shell entirely and acquiring reversed PE directions for a single b0 volume only. All these techniques approximately decrease the total acquisition time to its one-third. (b) The parameters for each gradient table is presented together with the number of shells and the specific b-vector distributions for each strategy. Each column corresponds to the undersampling technique applied for the R=2 case, but altered to achieve an acceleration rate of R=3.*
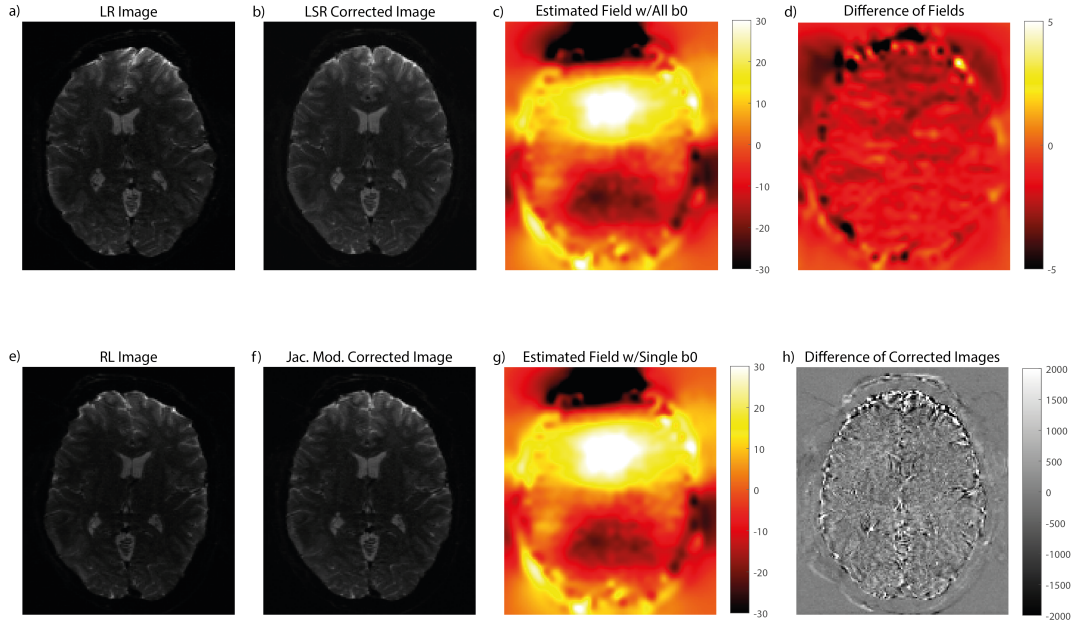
Figure 3.3: *Susceptibility induced artifact correction process. (a,e) For each q-space point, the dataset contained two volumes acquired in reversed PE directions (RL and LR). (b-c) The artifacts are corrected using the Least-Squares Restoration (LSR) technique, where the off-resonance field map is estimated from all pairs of b0 volumes with reversed PE directions. (f-g) It is also possible to perform this correction using the Jacobian modulation technique, where the off-resonance field map is estimated using a single b0 volume acquired in reversed PE direction. The diffusion-weighted volumes are acquired with a single PE direction (i.e., RL only). (d) The difference of estimated field maps obtained from all b0 volumes and a single b0 volume shows large deviations on the periphery of the brain. (h) The difference between the images corrected with the LSR and Jacobian modulation shows deviations between the two techniques especially in regions where their estimated field maps differ. In general, the Jacobian modulation correction produces images with reduced quality compared to the LSR correction.*

a) Brain Mask b) MD Map Masked w/Brain Mask c) CSF Segmentation Mask d) CSF Masked MD Map
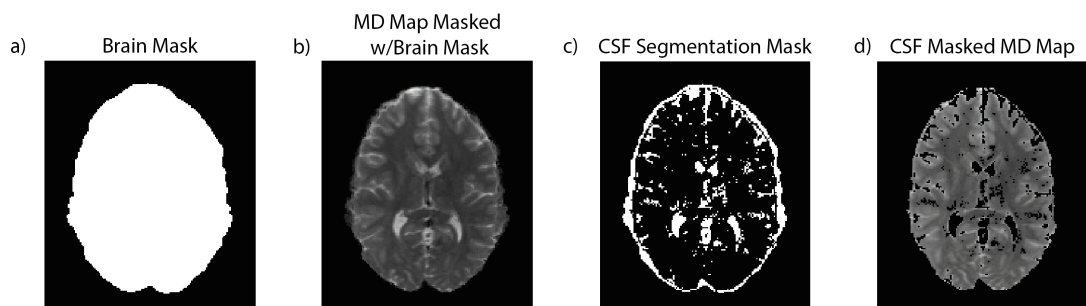
Figure 3.4: *(a) After the distortion correction, a binary brain mask is produced with FSL BET tool, (b) which is then used to suppress non-brain voxels and background noise to increase the accuracy of the quantitative quality assessments. (c) A CSF segmentation mask is generated with FSL FAST, (d) which is used for suppressing the CSF regions to increase the accuracy of quantitative quality assessments for WM and GM tissues. Here, the masking process is demonstrated on an MD map.*

Chapter 4

Results

4.1   Visual Comparisons

The metric maps together with the absolute error images corresponding to the axial middle slice for one of the subjects at the acceleration rate of R=2 are shown in Figs. 4.1, 4.2, and 4.3 for DTI, MSMT-CSD, and NODDI metrics, respectively. For R=3, the results for DTI, MSMT-CSD, and NODDI metrics for the same subject are shown in Figs. 4.4, 4.5, and 4.6, respectively. One can see that for both R=2 and R=3, a different undersampling strategy is preferred by each metric. For instance, based on the error images for R=2, the error increases for 2-shell strategies for nuFO and AFD, especially in CSF regions, while the errors in WM and GM regions are minimized with the strategy titled "10-15-20". For MD, the error in CSF regions is minimum for the "3-13-29" strategy, while the error increases similarly for the 2-shell strategies. For R=3, a similar behaviour is still observable. For ODI and NDI, the error is minimized for the "Single b0 TOPUP" strategy, whereas for MD the strategy producing the least error is the "2-9-19" strategy.

Overall, the metrics computed from the undersampled data preserve the structural tissue properties. In each metric map, WM, GM, and CSF regions can be

clearly delineated. The error images show that, especially for DTI and NODDI metrics, the error accumulates in CSF regions, while a homogeneous error distribution is observed in WM and GM regions. These observations indicate that the metric maps can still be used as biomarkers, since diffusion anisotropy and WM complexity can be visually resolved at a sufficient level using the undersampled data.

Comparing the performances of the undersampling strategies for R=2 versus R=3, one can see that the 3-shell strategies perform favorably at R=2, whereas 2-shell strategies are preferable at R=3. Note that 45 and 30 b-vectors were distributed over 3-shells or 2-shells for R=2 and R=3, respectively. At R=3, the number of b-vectors is not large enough to sample the highest order shell extensively enough while preserving the multi-shell sampling pattern. Hence, these results suggest that as the number of b-vectors decreases, having high SNR measurements becomes more important than having increased angular resolution.

Additionally, for all equivalent undersampling strategy pairs at R=2 and R=3, the strategies proposed for R=2 always outperform the strategies for R=3. This observation supports the expectation that a denser coverage of the q-space improves the quality of the metric maps.

4.2   Quantitative Comparisons

4.2.1   SSIM and PSNR Results

SSIM and PSNR were calculated for each metric map after suppressing the CSF regions. The median and interquartile-range (IQR) values for SSIM and PSNR computed across 20 subjects for R=2 are reported in Fig. 4.7 and Fig. 4.8, respectively. Likewise, SSIM and PSNR results for R=3 are reported in Fig. 4.10 and Fig. 4.11, respectively. Here, the best performing strategy for each metric is marked with green bold font, the second best strategy is marked in green regular font, the worst performing strategy is marked in red bold font, and the second

worst strategy is marked in red regular font. These results support the qualitative observation that for both R=2 and R=3, a different undersampling strategy is preferred by each metric. As expected, the SSIM and PSNR values obtained for R=2 are always higher than those for R=3, as the q-space coverage directly affects the accuracy of the estimated metrics.

For the acceleration rate of R=2, 3-shell strategies perform generally better than the competing strategies. Although 3-shell strategies are preferable on average, for FA, ODI, and nuFO, some of the 2-shell strategies still produce promising results, especially the ones labeled as "16-29" and "30-15". The "Single b0 TOPUP" strategy produces mediocre or even poor results compared to other strategies for the majority of the metrics, despite preserving the original q-space data with 89 b-vectors. The overall best performing strategy is the one titled "10-15-20", which has the highest (or the second highest) PSNR and SSIM values for the majority of the diffusion metrics.

For R=3, the trends observed at R=2 are reversed, such that the 2-shell strategies outperform the 3-shell strategies. The non-uniform 2-shell strategy titled "10-20" is the overall best performing strategy. Here, 30 b-vectors were distributed over 3- or 2-shells. Interestingly, the counterparts of the 3-shell strategies with poor performances for the R=2 case still perform poorly at R=3, producing the worst results overall. For example, for nuFO at R=2, "5-15-25" is the worst performing strategy with 0.823 SSIM and 19.43 dB PSNR. Its R=3 counterpart "5-10-15" again has the worst performance for nuFO, with further decreased SSIM and PSNR values of 0.750 and 17.61 dB, respectively. Similarly, the worst performance for ODI at R=2 is obtained under "3-13-29" with 23.89 db PSNR and 0.914 SSIM. Its R=3 counterpart "2-9-19" produces further decreased performance with an SSIM of 0.848 and PSNR of 21.21 dB. Note that for R=3, the counterpart of the best performing R=2 strategy titled "10-15-20" is the "7-10-13" strategy, which has a mediocre performance. This strategy has reduced SSIM and PSNR compared to its R=2 counterpart, and shows mediocre SSIM and PSNR values compared to the other R=3 strategies. Finally, the "Single b0 TOPUP" strategy produces decent performing results for several metrics such as nuFO and ODI, but produces the worst performing results for FA with increased

IQR values relative to other strategies.

4.2.2 JSD Results

JSD was computed for ODFs associated with DTI and MSMT-CSD analyses. Note that JSD was not computed for NODDI, as this technique is not based on orientation distribution but rather focuses on orientation dispersion by assuming a Watson distribution based axon-stick model. In NODDI analysis, ODI is the measure of the orientation dispersion, κ. Hence, evaluating the accuracy of the ODI metric suffices in the case of NODDI.

JSD measures the similarity between the reference ODF coefficients and those estimated from the undersampled data. To compute ODF for each, a sphere with 724 directions was utilized. JSD results for R=2 and R=3 are given in Figs. 4.9 and 4.12, respectively. A small JSD indicates a higher similarity between the compared ODFs, and therefore corresponds to a higher fidelity ODF estimation in the case of undersampling.

At R=2, the best performance in terms of DTI ODF retrieval, which is the ellipsoid constructed with the eigenvectors of the diffusion tensor, is the strategy labeled "3-13-29". This strategy provides the best performance for FA, and the worst performance for MD in terms of SSIM with the worst performance visually. It could be said that since the accuracy of ODF highly depends on diffusion anisotropy retrieval accuracy, there could be an agreement between the performances seen for FA and DTI ODF. For MSMT-CSD, the minimum JSD is obtained for the strategy titled "30-15", which is in accordance with the fact that the same strategy had the best performance for nuFO in terms of SSIM and PSNR. The second best performing strategy is "10-15-20", which is in accordance with the high performance of this strategy evaluated visually and quantitatively. The accuracy of AFD and nuFO metrics directly depend on the accuracy of ODF estimation. Since AFD is the magnitude of ODF peaks and nuFO is the number of ODF peaks, an error in the ODF estimation directly affects the accuracy of the metric maps. Therefore, for these metrics, JSD, PSNR, and SSIM results favor

similar strategies.

For ODF obtained with DTI analysis at R=3, the best performing strategy becomes the non-uniform 3-shell strategy titled "2-9-19", while the worst performing strategy is "20-10". The PSNR and SSIM metrics, together with the visual results suggested that the best strategy for MD is the same strategy "2-9-19", while for FA, which resolves the diffusion anisotropy in DTI, the best strategy was the ones titled "15-15" and "10-20", both consisting of 2 shells. Although for FA and MD the best performing strategy varies, the JSD results suggests that for ODF, the 3-shell "2-9-19" strategy better resolves the overall shape of the DTI ellipsoid when compared to the competing strategies. These results may suggest that although 2-shells strategies provide a good performance for measuring the average diffusivity in the tissue, they resolve a more sensitive diffusion orientation and fiber geometry than the fully sampled 3-shell case for the DTI analysis.

For ODF obtained with MSMT-CSD analysis at R=3, the best performance in terms of ODF retrieval with minimum JSD is achieved for the strategy titled "10-20". This result is consistent with the performances of metric maps in terms of visual inspection, as well as PSNR and SSIM results. The worst performing strategy is "5-10-15", which is also in accordance with the results obtained from the visual error maps, PSNR, and SSIM.

Overall, the JSD results for DTI analysis demonstrate poor performance when compared to the JSD results for MSMT-CSD analysis, as indicated with larger JSD values at both R=2 and R=3. These results suggest that MSMT-CSD, with its ability to resolve complex fibre structures and retrieve multiple fibre orientations, is more robust against undersampling. However, the DTI metrics FA and MD are more robust against undersampling, producing the highest PSNR and SSIM values at both R=2 and R=3.

Comparing the JSD results for R=2 and R=3, it is clear that the JSD values are always smaller at R=2 than at R=3. This results indicates that, as expected, the ODFs estimated estimated at R=2 better capture the underlying fibre distributions. Among all schemes at R=2, the strategy titled "10-15-20" is the overall

best performing strategy in terms of visual and quantitative analysis of metric maps and ODF accuracy. At R=3, the favorable choice is the "10-20" strategy, which provides a further accelerated multi-shell HARDI acquisition with slightly reduced but still acceptable performance. Importantly, both quantitative and visual analyses suggest that each metric prefers a different strategy, which further changes depending on the acceleration rate. Therefore, the best approach is to design the gradient tables based on the clinical study, the targeted neurodegenerative disease, and the targeted dMRI metric.
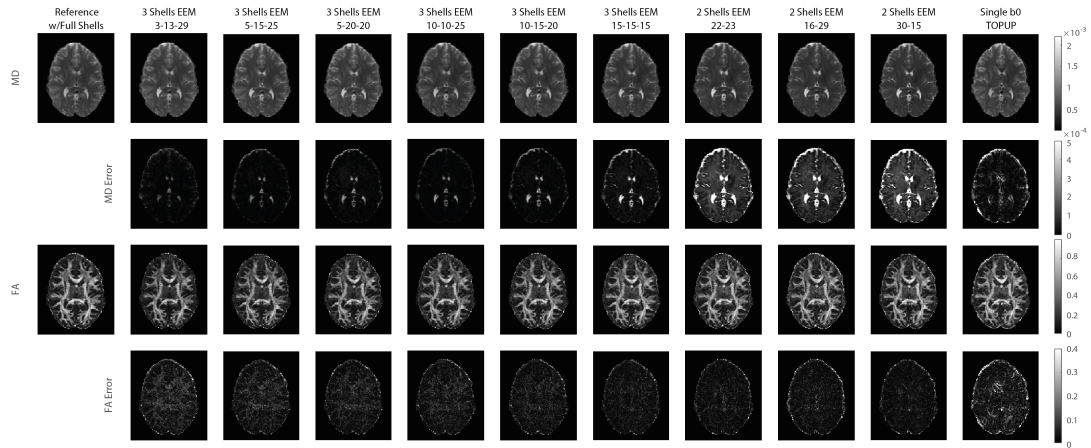
Figure 4.1: *MD and FA maps from DTI analysis using the undersampled multi-shell HARDI data for one of the subjects at R=2. The absolute error images show the errors with respect to the reference metric maps with the original 89 diffusion-weighted gradient directions.*
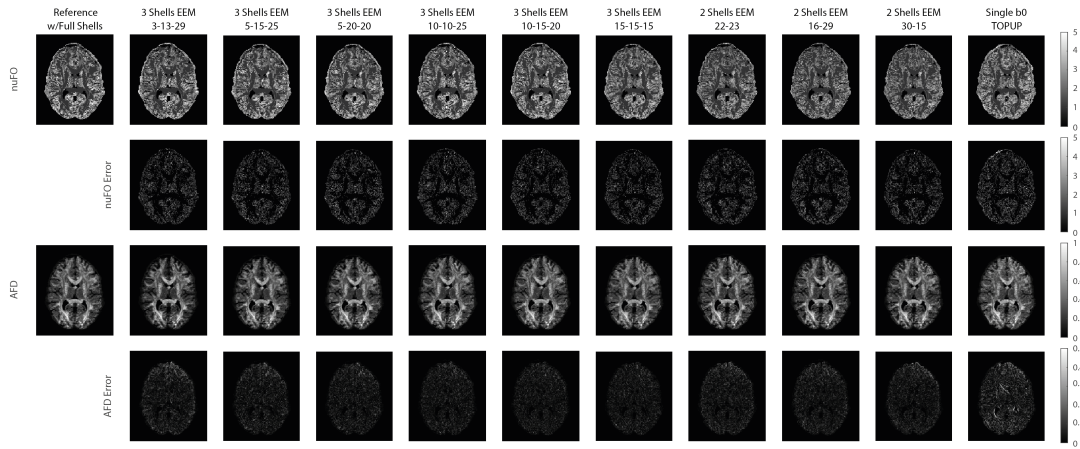
Figure 4.2: *nuFO and AFD maps obtained from MSMT-CSD analysis using the undersampled multi-shell HARDI data at R=2 for one of the subjects. Each metric map is shown with the corresponding absolute error image computed with respect to the reference metric maps with the original 89 diffusion-weighted gradient directions.*
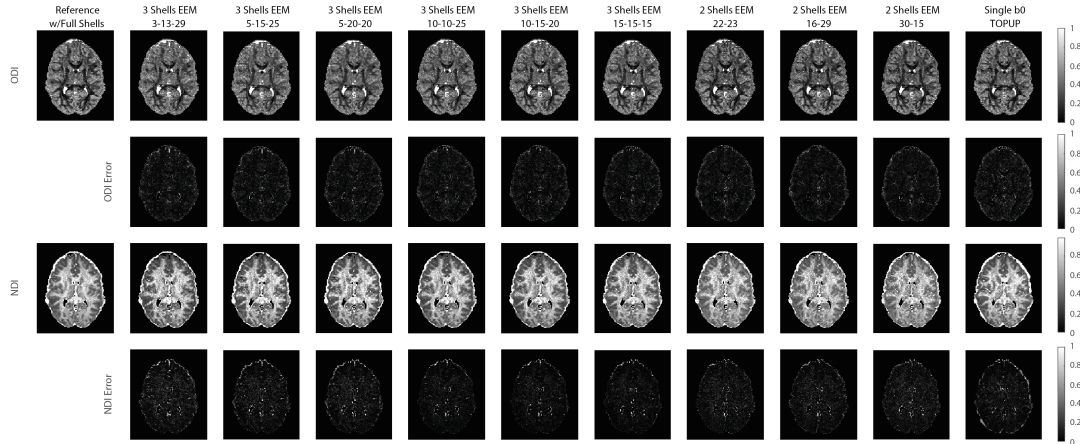
Figure 4.3: *ODI and NDI maps constructed with NODDI analysis using the undersampled multi-shell HARDI data at R=2, shown for one of the subjects. The absolute error image for each metric was computed with respect to the reference metric maps obtained with the original 89 diffusion-weighted gradient direction.*
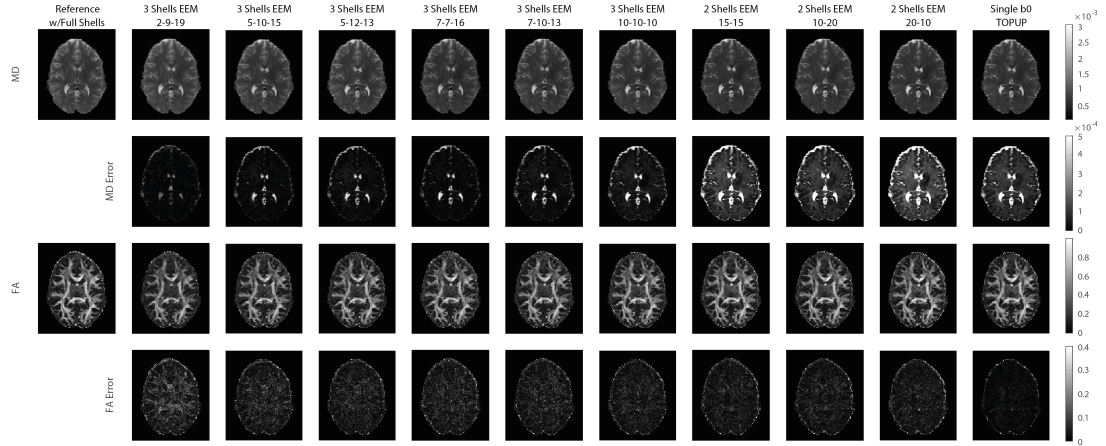
Figure 4.4: *MD and FA maps, obtained through DTI analysis of the undersampled multi-shell HARDI data for R=3. The metric maps and error images are shown for one of the subjects. The absolute error images compares the performances of undersampling strategies with respect to the reference, fully sampled case.*
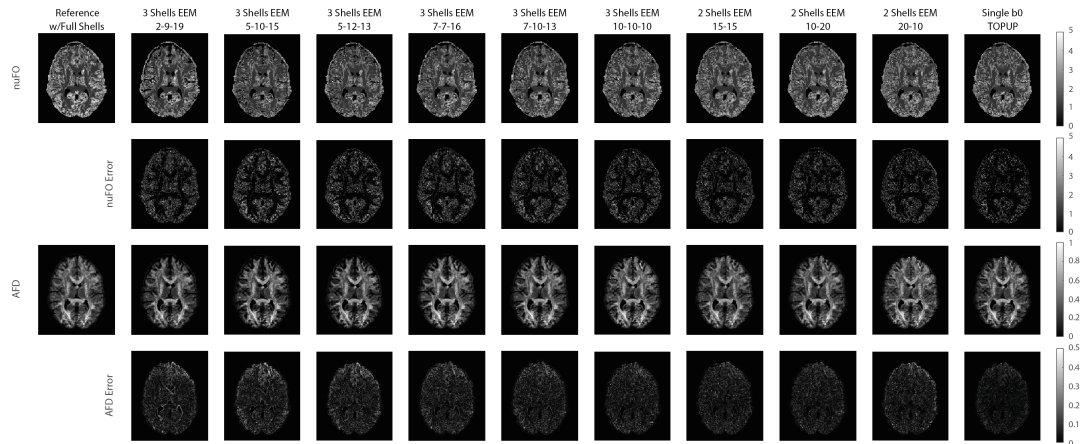
Figure 4.5: *nuFO and AFD maps from MSMT-CSD analysis using the undersampled multi-shell HARDI data for the case of R=3. Each metric map for the specific undersampling strategy is presented with the corresponding absolute error images, computed with respect to the reference fully sampled case.*
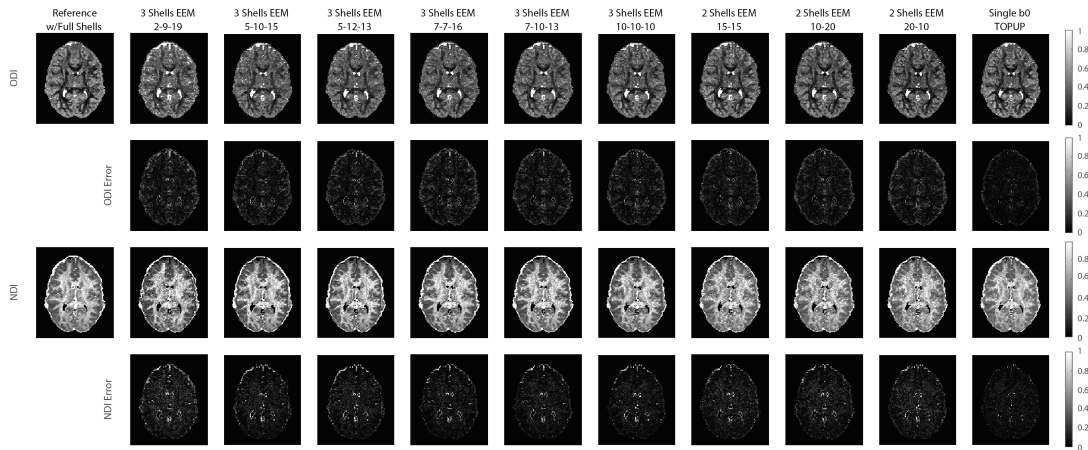
Figure 4.6: *ODI and NODDI maps computed with NODDI analysis using the undersampled multi-shell HARDI data for R=3. The first and third row corresponds to the metric maps of a subject chosen from the dataset, and the second and forth rows correspond to the absolute error images computed with respect to the reference metric maps, obtained from the fully sampled case.*

SSIM	3-13-29	5-15-25	5-20-20	10-10-25	10-15-20	15-15-15	22-23	16-29	30-15	Single b0 TOPUP
ODI	0.914 (0.028)	0.916 (0.027)	0.920 (0.021)	0.920 (0.023)	**0.930 (0.022)**	0.926 (0.028)	0.926 (0.009)	0.929 (0.015)	0.930 (0.034)	**0.903 (0.013)**
NDI	**0.877 (0.037)**	0.901 (0.031)	0.898 (0.029)	**0.936 (0.016)**	0.935 (0.018)	0.932 (0.036)	0.897 (0.016)	0.899 (0.040)	0.900 (0.050)	0.918 (0.017)
AFD	0.927 (0.026)	0.935 (0.015)	0.940 (0.015)	0.945 (0.009)	0.946 (0.010)	**0.948 (0.040)**	0.830 (0.030)	0.941 (0.008)	0.943 (0.016)	**0.814 (0.032)**
nuFO	0.826 (0.047)	**0.823 (0.033)**	0.834 (0.032)	0.841 (0.033)	0.843 (0.032)	0.848 (0.054)	0.827 (0.020)	0.840 (0.025)	**0.855 (0.029)**	0.830 (0.019)
MD	**0.947 (0.005)**	0.952 (0.008)	0.957 (0.005)	0.958 (0.002)	0.966 (0.010)	0.956 (0.017)	0.956 (0.003)	0.960 (0.004)	0.950 (0.007)	**0.968 (0.006)**
FA	**0.996 (0.002)**	0.996 (0.002)	0.994 (0.002)	0.996 (0.002)	0.994 (0.007)	0.990 (0.006)	0.970 (0.006)	0.965 (0.008)	0.973 (0.009)	**0.935 (0.011)**

Figure 4.7: *SSIM results of the undersampling strategies computed for R=2. SSIM of the undersampling strategies were computed for each subject, after CSF regions were supressed with a binary mask. For each metric, the median (interquartile range) for SSIM across 20 subjects is presented. The best performing strategy is presented in green bold font, the second best is presented in green regular font, the worst strategy is presented in red bold font, and the second worst strategy is presented in red regular font. Overall, the strategy titled "10-15-20" shows a favorable performance.*

PSNR (dB)	3-13-29	5-15-25	5-20-20	10-10-25	10-15-20	15-15-15	22-23	16-29	30-15	Single b0 TOPUP
ODI	**23.89 (0.60)**	24.12 (0.65)	24.39 (0.60)	24.35 (0.48)	24.69 (0.66)	24.59 (0.95)	24.88 (0.44)	**25.17 (0.40)**	24.82 (0.92)	24.04 (0.68)
NDI	**21.65 (0.98)**	22.82 (0.82)	22.68 (0.84)	24.97 (1.64)	**25.20 (1.76)**	24.78 (1.50)	23.83 (0.92)	22.68 (0.71)	22.38 (2.11)	24.11 (0.70)
AFD	26.70 (2.13)	28.09 (1.64)	28.41 (1.82)	29.05 (1.90)	**29.26 (1.04)**	28.98 (3.17)	19.59 (1.44)	29.11 (1.56)	28.49 (2.40)	**19.32 (0.84)**
nuFO	19.53 (1.11)	**19.43 (0.87)**	19.64 (0.89)	19.99 (0.89)	20.35 (0.90)	20.12 (0.92)	19.82 (1.26)	20.28 (1.13)	**20.58 (1.36)**	19.72 (1.87)
MD	27.38 (0.61)	28.29 (0.65)	28.79 (0.81)	29.58 (1.04)	30.50 (0.98)	**30.80 (1.80)**	27.70 (1.28)	25.83 (1.14)	**23.77 (0.73)**	33.39 (1.21)
FA	39.91 (1.30)	40.56 (1.74)	38.19 (1.90)	**40.82 (2.63)**	36.58 (4.39)	33.27 (1.40)	30.93 (0.98)	30.26 (0.73)	31.34 (1.16)	**27.43 (1.25)**

Figure 4.8: *PSNR results of the undersampling strategies computed for R=2. For each metric, the median (interquartile range) across 20 subjects is presented. PSNR was computed after the CSF regions were masked out with a binary tissue mask. The best performing strategies are presented with green bold font, while the worst performing strategies were presented in red bold font. Overall, the non-uniform 3-shell strategy titled "10-15-20" outperforms the other proposed strategies.*

					R=2					
	3-13-29	5-15-25	5-20-20	10-10-25	10-15-20	15-15-15	22-23	16-29	30-15	Single b0 TOPUP
MSMT-CSD	0.355 (0.052)	**0.372 (0.068)**	0.355 (0.062)	0.347 (0.055)	0.344 (0.058)	0.344 (0.045)	0.346 (0.032)	0.350 (0.030)	**0.323 (0.043)**	0.362 (0.011)
DTI	**0.433 (0.063)**	0.447 (0.071)	0.450 (0.084)	0.459 (0.070)	0.450 (0.078)	0.458 (0.079)	0.460 (0.069)	0.488 (0.080)	0.478 (0.068)	**0.524 (0.060)**

Figure 4.9: *JSD results for ODFs of MSMT-CSD and DTI analyses computed for R=2. For each case, the median (interquartile range) of JSD across 20 subjects is presented for ODFs computed using a sphere with 724 independent directions for all undersampling strategies. Smaller JSD indicates higher similarity to the reference ODF from the fully sampled case. The smallest JSD indicating the highest similarity is obtained for the 2-shell strategy titled "30-15" for MSMT-CSD, whereas the 3-shell strategy titled "10-15-20" has the second highest similarity. For DTI, the best ODF retrieval is achieved with the non-uniform 3-shell strategy titled "3-13-29".*

SSIM	2-9-19	5-10-15	5-12-13	7-7-16	7-10-13	10-10-10	15-15	10-20	20-10	Single b0 TOPUP
ODI	**0.848 (0.042)**	0.862 (0.044)	0.867 (0.043)	0.876 (0.041)	0.866 (0.041)	0.881 (0.042)	0.885 (0.042)	0.886 (0.041)	0.884 (0.027)	**0.887 (0.054)**
NDI	**0.815 (0.055)**	0.864 (0.046)	0.863 (0.050)	0.881 (0.051)	0.885 (0.051)	**0.888 (0.049)**	0.848 (0.058)	0.850 (0.062)	0.848 (0.056)	0.856 (0.062)
AFD	0.892 (0.025)	**0.884 (0.041)**	0.891 (0.029)	0.910 (0.031)	0.902 (0.028)	0.916 (0.024)	0.919 (0.026)	**0.925 (0.021)**	0.914 (0.027)	0.905 (0.076)
nuFO	0.767 (0.041)	**0.750 (0.066)**	0.753 (0.057)	0.786 (0.060)	0.776 (0.051)	0.789 (0.052)	0.814 (0.040)	0.809 (0.041)	**0.817 (0.046)**	0.809 (0.083)
MD	**0.992 (0.003)**	0.990 (0.003)	0.988 (0.003)	0.987 (0.004)	0.990 (0.003)	0.982 (0.003)	0.949 (0.01)	0.963 (0.007)	**0.933 (0.012)**	0.937 (0.037)
FA	0.930 (0.018)	0.944 (0.012)	0.946 (0.013)	0.942 (0.009)	0.941 (0.019)	0.951 (0.013)	0.953 (0.016)	**0.956 (0.011)**	0.951 (0.012)	**0.926 (0.063)**

Figure 4.10: *SSIM results of the undersampling strategies computed for R=3. The median (interquartile range) across 20 subjects is presented. Overall, the best performing strategy is the one titled "10-20", which is a non-uniform 2-shell undersampling strategy consisting of 30 non-diffusion weighted gradient directions.*

PSNR (dB)	2-9-19	5-10-15	5-12-13	7-7-16	7-10-13	10-10-10	15-15	10-20	20-10	Single b0 TOPUP
ODI	21.21 (0.51)	21.83 (0.63)	22.02 (0.70)	22.30(0.65)	21.91 (0.46)	22.42 (0.63)	22.71 (0.74)	22.82 (0.89)	22.45 (1.003)	22.76 (2.73)
NDI	19.18 (1.02)	21.13 (1.23)	20.94 (1.13)	21.72 (1.77)	21.63(1.78)	22.13 (1.81)	20.75 (1.41)	20.82 (1.55)	20.60 (1.13)	21.13 (2.16)
AFD	25.62 (1.76)	24.78 (1.60)	25.25 (1.27)	26.32 (1.42)	25.99 (1.60)	26.74 (1.92)	27.01 (2.05)	27.12 (1.11)	26.51 (2.15)	26.81 (3.60)
nuFO	18.51 (1.43)	17.61 (1.27)	18.00 (1.29)	18.41 (1.34)	18.42 (1.33)	18.86 (1.53)	19.58 (1.69)	19.41 (1.54)	19.60 (1.25)	20.16 (1.76)
MD	38.90 (1.71)	35.90 (1.96)	34.32 (1.41)	33.52 (1.60)	35.70 (1.83)	30.83 (1.29)	23.99 (1.05)	25.68 (1.09)	22.56 (1.51)	24.45 (1.59)
FA	26.10 (0.68)	27.64 (0.66)	28.02 (0.63)	28.01 (0.86)	27.85 (0.87)	28.90 (1.09)	29.07 (1.26)	28.97 (0.73)	28.80 (1.03)	26.97 (6.81)

Figure 4.11: *PSNR results of the undersampling strategies computed for R=3. The median (interquatile range) across 20 subjects is presented. Overall, the best performing strategy is the one titled "10-20", which consists of 30 non-diffusion weighted gradient directions non-uniformly distributed over 2 shells.*

	2-9-19	5-10-15	5-12-13	7-7-16	7-10-13	10-10-10	15-15	10-20	20-10	Single b0 TOPUP
R=3										
MSMT-CSD	0.420 (0.049)	0.422 (0.015)	0.410 (0.017)	0.417 (0.006)	0.401 (0.067)	0.399 (0.022)	0.385 (0.027)	0.375 (0.026)	0.379 (0.025)	0.394 (0.142)
DTI	0.441 (0.050)	0.451 (0.056)	0.448 (0.070)	0.457 (0.083)	0.455 (0.059)	0.441 (0.068)	0.459 (0.084)	0.453 (0.068)	0.482 (0.050)	0.481 (0.038)

Figure 4.12: *JSD results for ODFs of MSMT-CSD and DTI analyses computed for R=3. The median (interquartile range) of JSD across 20 subjects is presented. The best performing strategy in terms of ODF retrieval for MSMT-CSD with the minimum JSD is the one titled "10-20", which is a non-uniform 2-shell strategy. For DTI, the best ODF retrieval is achieved with the non-uniform 3-shell strategy titled "2-9-19", and the uniform 3-shell strategy titled "10-10-10" is a close second.*

Chapter 5

Discussion and Conclusion

In this thesis, several undersampling strategies were proposed and assessed to speed up multi-shell dMRI protocols by acceleration rates of R=22 and R=3. At R=2, the total acquisition time was reduced to 10 minutes, and at R=3, it was reduced to approximately 7 minutes. Two different approaches were utilized to decrease the total acquisition time: (1) The q-space data was directly undersampled with the EEM technique applied to each shell separately at different rates to reach different combinations for the number of b-vectors per shell. (2) The distortion correction was applied using the Jacobian modulation, which requires only a single b0 volume acquired in reversed PE directions to estimate the magnetic susceptibility off-resonance field coefficients, together with diffusion volumes acquired in a single PE direction. For R=2, this strategy decreases the total acquisition time to half. For R=3, this strategy was modified by discarding the 3rd shell to reduce the acquisition time to approximately one-third.

DTI, MSMT-CSD, and NODDI analyses were applied to retrieve the diffusion orientations, as well as to compute the dMRI metrics FA, MD, AFD, nuFO, ODI and NDI for 20 subjects. The visual comparisons of the metric maps and absolute error images suggest that both for acceleration rates of R=2 and R=3, the metric maps from the undersampled data preserve sufficient microstructural and anatomical information about the underlying neurites, especially in WM and

GM regions, for being used as biomarkers. In CSF regions, an error accumulation was observed especially in MD and NDI, which characterize mainly the diffusion magnitude and neurite density in the intra-neurite space.

These results suggest that the studies targeting to capture changes in CSF for indication of possible diseases could lose their efficacy while utilizing undersampled HARDI data. Because dMRI studies do not commonly investigate the diffusion characteristics in CSF regions, the error accumulation in those regions could be acceptable for many studies. In contrast, in GM and WM regions, the errors seem to be dispersed homogeneously and specific high-error regions were not observed. Overall, the metric maps computed in the case of undersampling can be said to preserve their fidelity and are therefore suitable for usage as biomarkers in the diagnosis of neurodegenerative diseases causing changes to the WM and GM areas.

Comparing the absolute error images obtained for a given metric under different undersampling strategies at the same acceleration rate, it is seen that overall error visibly increases for some strategies. For instance, for the "Single b0-volume TOPUP" approach, the error increases in FA and ODI metrics at R=2, while a smaller error is observed in MD. These results suggest that instead of choosing a single common strategy for all metrics, the specific metric should be considered while choosing the acceleration technique, as it is clear that each metric prefers a different strategy. For instance, visually, the absolute error is minimized for the strategy titled "3-13-29" and "2-9-19" for MD, while FA prefers strategies titled "3-13-29" and "single b0 TOPUP" at R=2 and R=3, respectively. This result depends on the fact that while FA measures the diffusion anisotropy and therefore the diffusion direction, MD measures the average diffusivity in a voxel. The benefit obtained from increased angular resolution and increased SNR in these two strategies creates the differences observed in the performances.

Comparing the visual results obtained from R=2 and R=3, it is seen that the metric maps are highly affected from the number of q-space measurements. The error increased for every undersampling strategy for every metric for the R=3 case. This observation becomes more prominent in CSF regions and the error

maps of the worst performing strategies.

PSNR and SSIM metrics are computed for each subject and median (interquartile range) across all subjects were reported. From the quantitative results, again, it is seen that the best performing strategy changes depending on the metric. Overall, comparing the metric-wise results, the 3-shell strategies performs better for R=2 compared to other approaches. Among the 3-shell strategies, the one titled "10-15-20" can be considered to be the best performing strategy. For R=3, however, the 2-shell strategies outperform other undersampling approaches, and the non-uniform strategy titled "10-20" can be considered to be the best performing one.

For PNSR values of R=2, there seems to be a general consensus about the best performing strategies, method-wise and metric-wise. In contrast, the best performing strategy changes for R=3 for each metric. For instance both NDI and ODI metrics of NODDI perform the best under the strategy titled "10-15-20" in terms of PSNR for the R=2 case, but ODI prefers the strategy titled "10-20" while NDI prefers "10-10-10" for the R=3 case. This increased variability in the best performing strategy as the acceleration rate increases, weakens the confidence in a common best strategy.

For the majority of the metrics at both R=2 and R=3 cases, the "Single b0 TOPUP" strategy, which achieves acceleration by changing the distortion correction technique, is not preferred. Overall, this strategy produces mediocre and even poor results. Therefore, to increase the visual and quantitative performance of the metrics, for each q-space point a pair of opposite PE directions should be acquired to be utilized in TOPUP to estimate the field map and to correct images using the LSR method. Undersampling the q-space directly should be the preferred approach to accelerate the multi-shell HARDI protocols. Here, one important remark is that for ODI and nuFO, "single b0 TOPUP" seems to produce relatively better results for R=3 case when compared to the alternative strategies. This could be the effect of having an increased number of b-vectors of 60. The other strategies at R=3 had a relatively small number of b-vectors of 30. In previous studies, it was shown that the ODF retrieval performance of gradient

44

tables with less than 45 b-vectors was not optimal, and they produced poor fiber tractography results [14]. Hence, the slight increase in performance of the "single b0 TOPUP" strategy might be because of the increased number of b-vectors, instead of the success of the Jacobian modulation distortion correction approach.

Both the visual and quantitative results show that DTI metrics, which are relatively low dimensional compared to MSMT-CSD and NODDI metrics that resolve diffusion characteristics into their specific components, are more robust against undersampling. Here, there exist approximately a 0.1 difference in SSIM, 10 dB difference in PSNR values between FA, MD, and other metrics. Even for the acceleration rate of R=3, MD and FA produce PSNR values of 38.90 dB and 29.07 dB and SSIM values of 0.956 and 0.992 for the best performing strategies, which can be considered very successful considering the high acceleration rate and low number of b-vectors.

To enhance the quantitative analysis, JSD was used to compare the ODFs retrieved from the undersampled data using the DTI and MSMT-CSD analyses. JSD directly compares the performances of these undersampling strategies to retrieve the diffusion propagator, compared to the indirect comparisons provided through the metric maps. This comparison is beneficial to understand how angular resolution is affected by the different undersampling approaches and also to analyze the accuracy of these techniques in resolving the fiber geometries and orientations.

For DTI, the best ODF retrieval performance is achieved with the strategies labeled as "3-13-29" and "2-9-19" at R=2 and R=3, respectively. The visual maps and quantitative SSIM and PSNR results suggest that for R=2, MD and FA perform their best for different strategies. For instance, in terms of visual metric maps, these two metrics have minimized error maps for the strategies titled "3-13-29" and "Single b0 TOPUP". In terms of SSIM, however, MD prefers "Single b0 TOPUP" while FA prefers "3-13-29". For R=3, these two metrics prefer the strategies titled "2-9-19" and "10-20", respectively, in terms of PSNR, SSIM, and visual results.

The contrast between JSD and other quantitative results may suggest that while certain strategies could provide good results in terms of the dMRI metrics, their ODF retrieval performances are not optimal. For MSMT-CSD, the minimum JSD for R=2 case is achieved for the non-uniform 3-shell strategy titled "30-15". MSMT-CSD analysis depends mostly on the angular resolution, since the main goal is to estimate orientation distribution in each voxel. The metrics derived from MSMT-CSD highly depends on ODF and its peaks and magnitudes, which agrees with the performance achieved for nuFO. The next best performing strategy in terms of JSD is "10-15-20", which is the overall best performing strategy.

At R=3 for DTI, the uniform 3-shell strategy titled "2-9-19" outperforms the 2-shell undersampling approaches in terms of JSD. DTI estimates the primary orientation from the diffusion tensor eigenvalues and eigenvectors, which determines the orientation of the diffusion ellipsoid. This ellipsoid is considered as the ODF and highly depends on q-space acquisitions. Both FA and MD are also derived from the diffusion tensor, but they are not directly affected by the accuracy of the diffusion orientation itself. FA measures the anisotropy of the diffusion, with high values signifying that a clear diffusion orientation exists. However, it does not measure the accuracy of the estimated fiber orientation. Hence, while FA performs well with the "10-20" or "15-15" strategies, these strategies do not capture the ODF well enough. At R=3 for MSMT-CSD, the best performance was obtained with a 2-shell strategy titled "10-20". Once again, this result supports the results obtained from PSNR, SSIM, and visual inspection results obtained for AFD and nuFO.

Considering the worst performing strategies in terms of JSD, most of the 3-shell non-uniform strategies produce mediocre and even poor results. These results suggest that for R=3, data utilizing a 3-shell approach is not sufficient to sample each diffusion shell densely enough for an accurate ODF estimation. Hence, 3-shell strategies become relatively unfeasible with low q-space coverage and the HARDI protocols lose both from SNR and angular resolution at the same time.

Comparing the R=2 and R=3 results together, it is concluded that ODF highly

depends on the number of q-space acquisition, as JSD is always lower at R=3 than at R=2. Although R=3 produces clinically acceptable metrics with relatively high structural integrity within an acceptable acquisition time, the ODFs lose their accuracy, which may affect more sophisticated applications. Note that the ODF accuracy also depends on the distortion correction approach. "single b0 TOPUP" approaches in both cases have higher q-space coverage with 89 and 60 b-vectors, respectively. However, they produce bad and even the worst results for some of the metrics. This observation supports the failure of "single b0 TOPUP" approaches in visual inspection, as well as in PSNR and SSIM analyses. While designing an accelerated HARDI protocol, it can be suggested that two volumes should be acquired in reversed PE directions and the undersampling should be performed in q-space directly.

For an acceleration rate of R=2, to achieve an overall well performing strategy, the gradient table should be designed to include three diffusion shells with a non-uniform distribution with low variance in the number of q-points between the consecutive shells. For R=3, the strategy should consist of non-uniform distribution of q-space points over two shells. Overall non-uniform strategies outperform uniform strategies, allowing high b-value shells with large surface areas to be sampled more extensively and thus benefiting from the increased angular resolution. It was observed from JSD results that ODFs are more accurately resolved for non-uniform 3-shells strategies for the R=2 case. If a multi-shell HARDI data will not to be used in tractography studies, which requires highly sensitive fiber distribution reconstructions, R=3 strategies can provide sufficient accuracy in terms of metric maps, as proven by visual inspection, PSNR, and SSIM. Thus, if the priority constraint is the total acquisition time, one can decide using R=3, by sacrificing from the ODF accuracy and angular resolution. Still, it is suggested to design the strategy based on the metric, clinical study, and diagnosed disease to achieve the best performance.

Quantitative metrics, providing beneficial analysis on the performances of undersampling strategies sometimes provide mediocre sensitivity. For instance, for the R=3 case, ODI has a range of SSIM values with a maximum difference between the worst and the best performing strategies of 1.61 dB and a minimum

difference of 0.05 dB. This signifies that the performance differences between some of the strategies are not significant enough. In contrast, MD, which is a low dimensional metric, has a PSNR difference ranging from 0.20 dB to 14.91 dB, allowing one to clearly assess the best performing strategy. Low dimensional metrics, providing a sharper difference in quantitative metrics, produce distinguishable results and are more robust against undersampling. For SSIM, a similar trend is observed. Among the metrics and strategies, a maximum difference of 0.073 and a minimum difference of 0.001 is observed. For JSD, a maximum difference of 0.055 and a minimum difference of 0.003 was observed. These values are distinguishable in the sense that the best and the worst performing strategies could be identified, and there exist at least 0.027 difference in JSDs between R=2 and R=3 strategies. Nonetheless, the sensitivity of JSD alone could only detect a slight difference in the performances. Although the best and the worst performing strategies can still be clearly identified based on the SSIM, PSNR, and JSD metrics, the performances of the remaining strategies are harder to rank by looking only at the quantitative metrics.

In conclusion, this thesis proposes and analyzes 20 different undersampling approaches at two different acceleration rates. The results will be beneficial for future designs of gradient tables for clinical studies aiming to diagnose a specific disease using multi-shell dMRI metrics as biomarkers, within a significantly reduced acquisition time.

Bibliography

[1] R. Bammer, "Basic principles of diffusion-weighted imaging," *European Journal of Radiology*, vol. 45, no. 3, pp. 169–184, 2003.

[2] M. Descoteaux, *High Angular Resolution Diffusion MRI: from Local Estimation to Segmentation and Tractography*. Theses, Université Nice Sophia Antipolis, Feb. 2008.

[3] P. J. Basser and E. Özarslan, "Chapter 1 - introduction to diffusion mr," in *Diffusion MRI (Second Edition)* (H. Johansen-Berg and T. E. Behrens, eds.), pp. 3–9, San Diego: Academic Press, second edition ed., 2014.

[4] M. Descoteaux, *High Angular Resolution Diffusion Imaging (HARDI)*, pp. 1–25. John Wiley Sons, Ltd, 2015.

[5] J.-D. Tournier, F. Calamante, and A. Connelly, "Robust determination of the fibre orientation distribution in diffusion mri: Non-negativity constrained super-resolved spherical deconvolution," *NeuroImage*, vol. 35, no. 4, pp. 1459–1472, 2007.

[6] S. By, J. Xu, B. A. Box, F. R. Bagnato, and S. A. Smith, "Application and evaluation of noddi in the cervical spinal cord of multiple sclerosis patients," *NeuroImage: Clinical*, vol. 15, pp. 333–342, 2017.

[7] A. Crombe, V. Planche, G. Raffard, J. Bourel, N. Dubourdieu, A. Panatier, H. Fukutomi, V. Dousset, S. Oliet, B. Hiba, and T. Tourdias, "Deciphering the microstructure of hippocampal subfields with in vivo dti and noddi: Applications to experimental multiple sclerosis," *NeuroImage*, vol. 172, pp. 357–368, 2018.

[8] G. P. Winston, C. Micallef, M. R. Symms, D. C. Alexander, J. S. Duncan, and H. Zhang, "Advanced diffusion imaging sequences could aid assessing patients with focal cortical dysplasia and epilepsy," *Epilepsy Research*, vol. 108, no. 2, pp. 336–339, 2014.

[9] J. Goveas, L. O'Dwyer, M. Mascalchi, M. Cosottini, S. Diciotti, S. De Santis, L. Passamonti, C. Tessa, N. Toschi, and M. Giannelli, "Diffusion-mri in neurodegenerative disorders," *Magnetic Resonance Imaging*, vol. 33, no. 7, pp. 853–876, 2015.

[10] J. Cheng, D. Shen, and P.-T. Yap, "Joint k-q Space Compressed Sensing for Accelerated Multi-Shell Acquisition and Reconstruction of the diffusion signal and Ensemble Average Propagator," in *ISMRM*, (Italy), p. 664, May 2014.

[11] D. Karimi, L. Vasung, C. Jaimes, F. Machado-Rivas, S. K. Warfield, and A. Gholipour, "Learning to estimate the fiber orientation distribution function from diffusion-weighted mri," *NeuroImage*, vol. 239, p. 118316, 2021.

[12] Y. Rathi, O. Michailovich, K. Setsompop, S. Bouix, M. E. Shenton, and C. F. Westin, "Sparse multi-shell diffusion imaging," in *Medical Image Computing and Computer-Assisted Intervention – MICCAI 2011* (G. Fichtinger, A. Martel, and T. Peters, eds.), (Berlin, Heidelberg), pp. 58–65, Springer Berlin Heidelberg, 2011.

[13] Y. Rathi, O. Michailovich, F. Laun, K. Setsompop, P. Grant, and C.-F. Westin, "Multi-shell diffusion signal recovery from sparse measurements," *Medical Image Analysis*, vol. 18, no. 7, pp. 1143–1156, 2014.

[14] J.-D. Tournier, F. Calamante, and A. Connelly, "Determination of the appropriate b value and number of gradient directions for high-angular-resolution diffusion-weighted imaging," *NMR in Biomedicine*, vol. 26, no. 12, pp. 1775–1786, 2013.

[15] D. C. Alexander and G. J. Barker, "Optimal imaging parameters for fiber-orientation estimation in diffusion mri," *NeuroImage*, vol. 27, no. 2, pp. 357–367, 2005.

[16] J.-D. Tournier, S. Mori, and A. Leemans, "Diffusion tensor imaging and beyond," *Magnetic Resonance in Medicine*, vol. 65, no. 6, pp. 1532–1556, 2011.

[17] V. Wedeen, T. Reese, M. W. D. Tuch, J.-G. Dou, R. Weiskoff, and D. Chessler, "Mapping fiber orientation spectra in cerebral white matter with fourier-transform diffusion mri," in *Proceedings of the International Society of Magnetic Resonance in Medicine*, p. 82, 2000.

[18] J.-D. Tournier, F. Calamante, D. G. Gadian, and A. Connelly, "Direct estimation of the fiber orientation density function from diffusion-weighted mri data using spherical deconvolution," *NeuroImage*, vol. 23, no. 3, pp. 1176–1185, 2004.

[19] B. Jeurissen, J.-D. Tournier, T. Dhollander, A. Connelly, and J. Sijbers, "Multi-tissue constrained spherical deconvolution for improved analysis of multi-shell diffusion mri data," *NeuroImage*, vol. 103, pp. 411–426, 2014.

[20] H. Zhang, T. Schneider, C. A. Wheeler-Kingshott, and D. C. Alexander, "Noddi: Practical in vivo neurite orientation dispersion and density imaging of the human brain," *NeuroImage*, vol. 61, no. 4, pp. 1000–1016, 2012.

[21] G. P. Winston, C. Micallef, M. R. Symms, D. C. Alexander, J. S. Duncan, and H. Zhang, "Advanced diffusion imaging sequences could aid assessing patients with focal cortical dysplasia and epilepsy," *Epilepsy Research*, vol. 108, no. 2, pp. 336–339, 2014.

[22] Q. Wen, D. A. Kelley, S. Banerjee, J. M. Lupo, S. M. Chang, D. Xu, C. P. Hess, and S. J. Nelson, "Clinically feasible noddi characterization of glioma using multiband epi at 7 t," *NeuroImage: Clinical*, vol. 9, pp. 291–299, 2015.

[23] T. Taoka, N. Aida, Y. Fujii, K. Ichikawa, H. Kawai, T. Nakane, R. Ito, and S. Naganawa, "White matter microstructural changes in tuberous sclerosis: Evaluation by neurite orientation dispersion and density imaging (noddi) and diffusion tensor images," *Scientific Reports*, vol. 10, p. 436, Jan 2020.

[24] M. Bozzali, A. Falini, M. Franceschi, M. Cercignani, M. Zuffi, G. Scotti, G. Comi, and M. Filippi, "White matter damage in alzheimer's disease assessed in vivo using diffusion tensor magnetic resonance imaging," *Journal of Neurology, Neurosurgery & Psychiatry*, vol. 72, no. 6, pp. 742–746, 2002.

[25] S. E. Rose, K. L. McMahon, A. L. Janke, B. O'Dowd, G. de Zubicaray, M. W. Strudwick, and J. B. Chalk, "Diffusion indices on magnetic resonance imaging and neuropsychological performance in amnestic mild cognitive impairment," *Journal of Neurology, Neurosurgery & Psychiatry*, vol. 77, no. 10, pp. 1122–1128, 2006.

[26] D. Van Essen, K. Ugurbil, E. Auerbach, D. Barch, T. Behrens, R. Bucholz, A. Chang, L. Chen, M. Corbetta, S. Curtiss, S. Della Penna, D. Feinberg, M. Glasser, N. Harel, A. Heath, L. Larson-Prior, D. Marcus, G. Michalareas, S. Moeller, R. Oostenveld, S. Petersen, F. Prior, B. Schlaggar, S. Smith, A. Snyder, J. Xu, and E. Yacoub, "The human connectome project: A data acquisition perspective," *NeuroImage*, vol. 62, no. 4, pp. 2222–2231, 2012. Connectivity.

[27] J. L. Andersson, S. Skare, and J. Ashburner, "How to correct susceptibility distortions in spin-echo echo-planar images: application to diffusion tensor imaging," *NeuroImage*, vol. 20, no. 2, pp. 870–888, 2003.

[28] "Advances in functional and structural mr image analysis and implementation as fsl," *NeuroImage*, vol. 23, pp. S208–S219, 2004. Mathematics in Brain Imaging.

[29] D. Jones, M. Horsfield, and A. Simmons, "Optimal strategies for measuring diffusion in anisotropic systems by magnetic resonance imaging," *Magnetic Resonance in Medicine*, vol. 42, no. 3, pp. 515–525, 1999.

[30] D. Jones, M. Horsfield, and A. Simmons, "Optimal strategies for measuring diffusion in anisotropic systems by magnetic resonance imaging," *Magnetic Resonance in Medicine*, vol. 42, no. 3, pp. 515–525, 1999.

[31] S. M. Smith, "Fast robust automated brain extraction," *Human Brain Mapping*, vol. 17, no. 3, pp. 143–155, 2002.

[32] J. Veraart, D. S. Novikov, D. Christiaens, B. Ades-aron, J. Sijbers, and E. Fieremans, "Denoising of diffusion mri using random matrix theory," *NeuroImage*, vol. 142, pp. 394–406, 2016.

[33] E. Garyfallidis, M. Brett, B. Amirbekian, A. Rokem, S. Van Der Walt, M. Descoteaux, and I. Nimmo-Smith, "Dipy, a library for the analysis of diffusion mri data," *Frontiers in Neuroinformatics*, vol. 8, 2014.

[34] D. K. Jones and M. Cercignani, "Twenty-five pitfalls in the analysis of diffusion mri data," *NMR in Biomedicine*, vol. 23, no. 7, pp. 803–820, 2010.

[35] Y. Zhang, M. Brady, and S. Smith, "Segmentation of brain mr images through a hidden markov random field model and the expectation-maximization algorithm," *IEEE Transactions on Medical Imaging*, vol. 20, no. 1, pp. 45–57, 2001.

[36] A. Daducci, E. J. Canales-Rodríguez, H. Zhang, T. B. Dyrby, D. C. Alexander, and J.-P. Thiran, "Accelerated microstructure imaging via convex optimization (amico) from diffusion mri data," *NeuroImage*, vol. 105, pp. 32–44, 2015.

[37] Z. Wang, A. Bovik, H. Sheikh, and E. Simoncelli, "Image quality assessment: from error visibility to structural similarity," *IEEE Transactions on Image Processing*, vol. 13, no. 4, pp. 600–612, 2004.

[38] J. Lin, "Divergence measures based on the shannon entropy," *IEEE Transactions on Information Theory*, vol. 37, no. 1, pp. 145–151, 1991.